

TURBULENT SEPARATION CONTROL EFFECTS OF MAKO SHARK SKIN SAMPLES
ON A NACA 4412 HYDROFOIL

by

JONATHON ANDREW SMITH

AMY W. LANG, COMMITTEE CHAIR

SEMIH M. OLCMEN

AJAY K. AGRAWAL

A THESIS

Submitted in partial fulfillment of the requirements for the
degree of Master of Science in the Department of
Aerospace Engineering and Mechanics
in the Graduate School of the
University of Alabama

TUSCALOOSA, ALABAMA

2011

Copyright Jonathon Andrew Smith 2011

ALL RIGHTS RESERVED

ABSTRACT

Shark skin is investigated as a means of passive flow separation control due to its preferential flow direction and the potential for its scales to obstruct low-momentum backflow resulting from an adverse pressure gradient. In this study, the effect of the scales on flow reversal is observed in a tripped turbulent boundary layer by comparing the flow over a NACA 4412 hydrofoil with a smooth, painted surface to that over the same hydrofoil with samples of mako shark skin affixed to its upper surface. These samples were taken from the shark's flank region because the scales at that location have been shown to have the greatest angle of bristling, and thus the best potential for separation control. All sets of flow data in this study were obtained using Time-Resolved Digital Particle Image Velocimetry and recorded at multiple angles of attack (between 8 and 16 degrees) and two Reynolds numbers. The flow was primarily analyzed by means of the backflow coefficient (a value based on the percentage of time that flow in a region over the hydrofoil is reversed), average backflow magnitude, and the time history of instantaneous flow velocity values at specific points in the boundary layer over the hydrofoil models. Results showed that at $\alpha=12^\circ$ and below, the shark skin generated a slightly larger, higher magnitude region of reversed flow than was seen over the painted surface. At $\alpha=16^\circ$, the backflow region of the shark skin surface was significantly reduced in size and magnitude compared to that of the painted surface. These results support the hypothesis that in order for the scales to be an effective means of flow control, sufficient shear must be present in the backflow to cause them to bristle fully.

LIST OF ABBREVIATIONS AND SYMBOLS

α	Hydrofoil angle of attack
γ_{pu}	Time fraction of downstream-moving flow
δ	Boundary layer thickness
τ_w	Average wall shear stress
c	Hydrofoil chord length
d	Test section water depth
h_{sr}	Height of 10% backflow line above surface
Re_L	Reynolds number based on chord length
U	Free stream velocity upstream of hydrofoil model
u	Mean velocity in the tangential direction of the local flow
u'	Instantaneous velocity fluctuation in the tangential direction of the local flow
$ u_b _{avg}$	Average backflow velocity magnitude in the x-direction of the flow
$ u_b _{max}$	Peak backflow velocity magnitude in the x-direction of the flow
v	Mean velocity in the normal direction of the local flow

ACKNOWLEDGMENTS

I would like to thank Dr. Amy Lang, my project mentor and committee chair, for her input and guidance on this project, and for allowing me the opportunity to participate in this research. I also thank Dr. Ajay Agrawal and Dr. Semih Olcmen for serving on my thesis committee. I am grateful for the assistance and support, in both conceptual planning and the conducting of experiments, of my fellow students in the water tunnel lab: Nikki Wheelus, Emily Jones, and Michael Bradshaw. I also would like to thank Dr. Redha Wahidi for his insight and suggestions into the analysis of my research. I am grateful for the guidance and direct help of Dr. Phillip Motta and Laura Habegger of the University of South Florida in the preparation and usage of the shark skin samples. I would like to acknowledge the work of the engineering machine shop in the design and construction of the models used in these experiments. I also greatly appreciate the financial support of the University of Alabama Graduate Council and the National Science Foundation during the course of my graduate education.

TABLE OF CONTENTS

ABSTRACT.....	ii
LIST OF ABBREVIATIONS AND SYMBOLS.....	iii
ACKNOWLEDGMENTS.....	iv
LIST OF FIGURES.....	vi
LIST OF TABLES.....	ix
1. INTRODUCTION.....	1
1.1 TURBULENT BOUNDARY LAYER SEPARATION.....	1
1.2 SHARK SKIN AS A MEANS OF FLOW CONTROL.....	3
1.3 OBJECTIVES.....	6
2. REVIEW OF LITERATURE.....	9
2.1 TURBULENT BOUNDARY LAYER SEPARATION.....	9
2.2 PASSIVE SEPARATION CONTROL.....	12
2.3 FLOW CONTROL MECHANISMS OF SHARK SKIN.....	14

3. EXPERIMENTAL SETUP.....	18
3.1 EXPERIMENTAL FACILITY.....	18
3.2 EXPERIMENTAL MODEL.....	19
3.3 DPIV SYSTEM.....	24
3.4 EXPERIMENTAL PROCEDURE.....	27
4. RESULTS AND DISCUSSION.....	34
4.1 MEAN VELOCITY FIELD.....	34
4.2 BACKFLOW COEFFICIENT.....	35
4.3 10 PERCENT FREE STREAM BACKFLOW.....	40
4.4 AVERAGE AND PEAK BACKFLOW MAGNITUDE.....	43
4.5 INSTANTANEOUS VELOCITY VS. TIME.....	46
4.6 RESULTS FOR MEASUREMENT PLANES AT 75% DEPTH.....	48
4.7 RESULTS FOR 50 CM/S FREE STREAM SPEED.....	50
4.8 DETERMINATION OF TURBULENCE.....	52
4.9 COMPARISON OF AVERAGES.....	54
5. CONCLUSIONS.....	56
5.1 SEPARATION CONTROL EFFECTS OF SHARK SKIN.....	56

5.2 REYNOLDS NUMBER DEPENDENCY.....	58
5.3 FUTURE WORK.....	59
REFERENCES.....	60
APPENDIX - UNCERTAINTY ANALYSIS.....	62

LIST OF FIGURES

1. Comparison of traditional and current views of TBL separation (Simpson, 1996).....	3
2. SEM of non-bristled mako scales (Lang et al., 2011).....	4
3. SEM of bristled mako scales (Lang et al., 2011).....	5
4. Diagram of measured scale bristling angles (Lang et al., 2011).....	5
5. SEM of individual scales (Lang et al., 2011).....	17
6. University of Alabama water tunnel facility.....	19
7. AoA selection dial on hydrofoil pivot plate.....	20
8. NACA 4412 hydrofoil model and mounting system, painted surface.....	21
9. NACA 4412 hydrofoil model, shark skin surface.....	22
10. Trailing edge of center shark skin sample.....	23
11. Top-down diagram of experimental setup.....	25
12. Basler high-speed camera and Quantronix pulsed laser.....	26
13. Diagram of measurement window locations.....	29
14. Chordwise ridges on center shark skin sample.....	31

15. Mean velocity field, Re=100,000, $\alpha=16^\circ$, Location 5.....	35
16. Backflow coefficient, Re=100,000, $\alpha=8^\circ$, Location 5.....	37
17. Backflow coefficient, Re=100,000, $\alpha=10^\circ$, Location 5.....	38
18. Backflow coefficient, Re=100,000, $\alpha=12^\circ$, Location 5.....	39
19. Backflow coefficient, Re=100,000, $\alpha=16^\circ$, Locations 3-5.....	40
20. 10% free stream backflow coefficient, Re=100,000, $\alpha=12^\circ$, Location 5.....	41
21. 10% free stream backflow coefficient, Re=100,000, $\alpha=16^\circ$, Location 4.....	42
22. Average backflow magnitude, Re=100,000, $\alpha=12^\circ$, Location 5.....	44
23. Average backflow magnitude, Re=100,000, $\alpha=16^\circ$, Location 5.....	45
24. Peak backflow magnitude, Re=100,000, $\alpha=16^\circ$, Location 4.....	46
25. Instantaneous velocity history, Re=100,000, $\alpha=12^\circ$, 95% chord.....	47
26. Instantaneous velocity history, Re=100,000, $\alpha=16^\circ$, 95% chord.....	48
27. Backflow coefficient, Re=100,000, $\alpha=10^\circ$, trailing edge, 75% depth.....	49
28. Backflow coefficient, Re=100,000, $\alpha=12^\circ$, trailing edge, 75% depth.....	50
29. Instantaneous u field, Re=152,000, $\alpha=16^\circ$, Location 5.....	51
30. Backflow coefficient, Re=152,000, $\alpha=16^\circ$, Location 5.....	52
31. Instantaneous velocity history, Re=100,000, $\alpha=10^\circ$, 30% chord.....	53

32. Backflow coefficient, Re=100,000, $\alpha=16^\circ$, Location 5, 4800 v. 7200 images.....55

LIST OF TABLES

1. Starting positions of measurement window locations.....	28
2. Image length scale calibration values and fields of view.....	32
3. $Re_L=100,000$ results for locations of ITD & D, and h_{sr}	36
4. Measurement window locations of backflow regions.....	36

1. INTRODUCTION

1.1 TURBULENT BOUNDARY LAYER SEPARATION

When flow over a surface encounters an adverse pressure gradient, whether it is due to the shape of the object or its orientation in the current flow conditions, the potential for the separation of its boundary layer presents a challenge to the optimization of the performance of the vehicle or object over which the flow is moving. This is because a separated boundary layer results in a significant increase in the pressure drag on the surface as well as a large decrease in the effectiveness of control surfaces located within the separated region, due to a sharp increase in the size of the rotational flow region near the surface and much larger values of the flow velocity perpendicular to the surface. For example, the stall angle of an airfoil, at which point the boundary layer has separated from the majority of its upper surface, is the orientation at which the airfoil can no longer produce increasing lift and does not respond to inputs from changes in trailing-edge control surfaces such as flaps or ailerons. Therefore, the separation associated with the stall angle represents the upper limit of an airfoil's performance, and the performance of the aircraft on which it is applied. For this reason, much research has been devoted to the control or reduction of boundary layer separation as well as providing a greater understanding of its occurrence and characteristics.

In the case of a laminar boundary layer, flow separation begins at a single point where the adverse pressure gradient has resulted in zero shear stress at the wall, and, consequently, the reversal of flow direction in the region immediately above the wall. At all locations past this

point of separation, the positive-direction flow is detached from the surface until the point of reattachment, resulting in a stationary separation bubble for a given configuration. The separation of a turbulent boundary layer adds additional complexity to the flow behavior. Because of its time-dependent nature, a turbulent boundary layer begins to separate intermittently at a point, meaning the flow at that point only reverses direction a small percentage of the time. From this point onward, the percentage of time during which flow is reversed increases. Since there is no single stationary point marking the onset of flow separation, Simpson (1989) gives a set of quantitative definitions to accompany backflow percentages of significant importance. Incipient detachment (ID, $\gamma_{pu}=0.99$) is defined as the point at which the time-averaged flow reverses direction during 1% of the total amount of time over which the set of flow data was obtained. Similarly, intermittent transitory detachment (ITD, $\gamma_{pu}=0.80$) occurs at the location where 20% percent instantaneous flow reversal is observed. The locations of transitory detachment (TD, $\gamma_{pu}=0.50$) and detachment (D), which are defined as the locations of 50% backflow and zero wall shear stress ($\tau_w=0$), respectively, have been shown to occur at the same point. The determination of these locations is important for mapping out the process of turbulent separation over a surface.

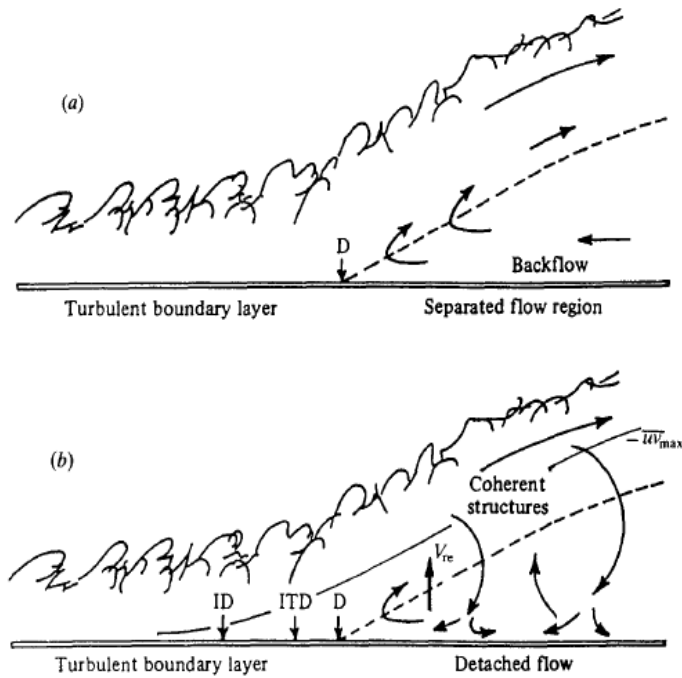


Figure 1.1 (a) Traditional view of turbulent boundary layer separation. (b) Currently accepted view, showing points of quantitative definitions of reversed flow percentages (Simpson, 1989).

1.2 SHARK SKIN AS A MEANS OF FLOW CONTROL

Nature's approach to flow control has long been a subject of interest in the field of fluid mechanics. From feathers on a bird, to scales on a butterfly's wing, to the skin of marine creatures such as fish, dolphins, and sharks, biological solutions to aerodynamics and hydrodynamics almost always differ from the hard, smooth surfaces employed in most engineering applications. However, relatively little quantitative research has been performed to determine what benefits could be gained by the employment of these biological surface patterns, due to their often complex three-dimensional nature. With the use of flow measurement techniques such as particle image velocimetry, it has become possible to analyze the flow over such surface geometries and compare the results with those of more conventional surfaces. One particular biological surface pattern, the skin of the Shortfin Mako shark (*Isurus oxyrinchus*), has

been the focus of research for several years in the University of Alabama water tunnel laboratory.

The Shortfin Mako is one of the fastest-swimming marine creatures, with burst speeds of over 20 meters per second having been recorded (Videler, 1995). Observation and underwater video have also shown that these sharks are extremely agile and maneuverable, capable of very sharp changes in direction at high speeds in rapid succession. The body of the mako shark has a sleek, torpedo-like profile to minimize drag. Additionally, it has been suggested the scales covering the shark's body could be a source of further drag reduction and flow separation control (Bechert, 2000). These scales, also known as denticles, have a similar morphology to teeth, with a hard outer layer encasing a softer core supplied with blood. Scanning electron microscope (SEM) images by Lang et al. (2011) show in detail the highly three-dimensional geometry of each scale (Figure 1.2). While the sizes of the scales differ from species to species, the scales of the Shortfin Mako measure approximately 0.2 mm in length from base to tip, at all locations on the shark's body. The scales are positioned in staggered rows with overlap between the tips of the scales on one row and the bases of the scales on the following row.

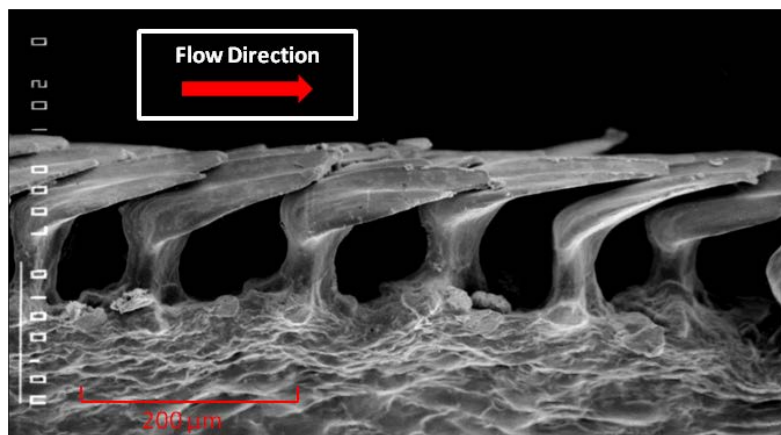


Figure 1.2 SEM of non-bristled mako scales, side view, preferred flow direction left to right.

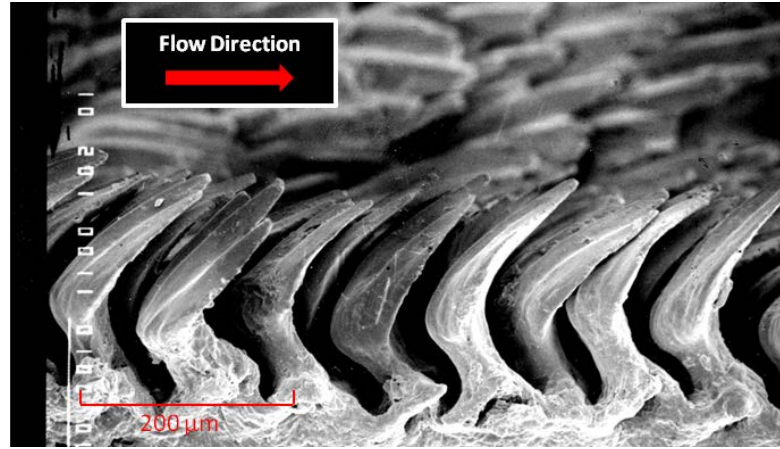


Figure 1.3 SEM of bristled mako scales, note formation of cavities between rows.

Recent work by Lang et al. (2011) has shown that the scales can be bristled to varying angles, depending on their location on the shark's body. It has been found that the most flexible scales are located along the flank of the shark, with maximum bristling angles of approximately 50 degrees with respect to the surface of the skin. A diagram of these bristling angles and their locations is shown in Figure 1.4.

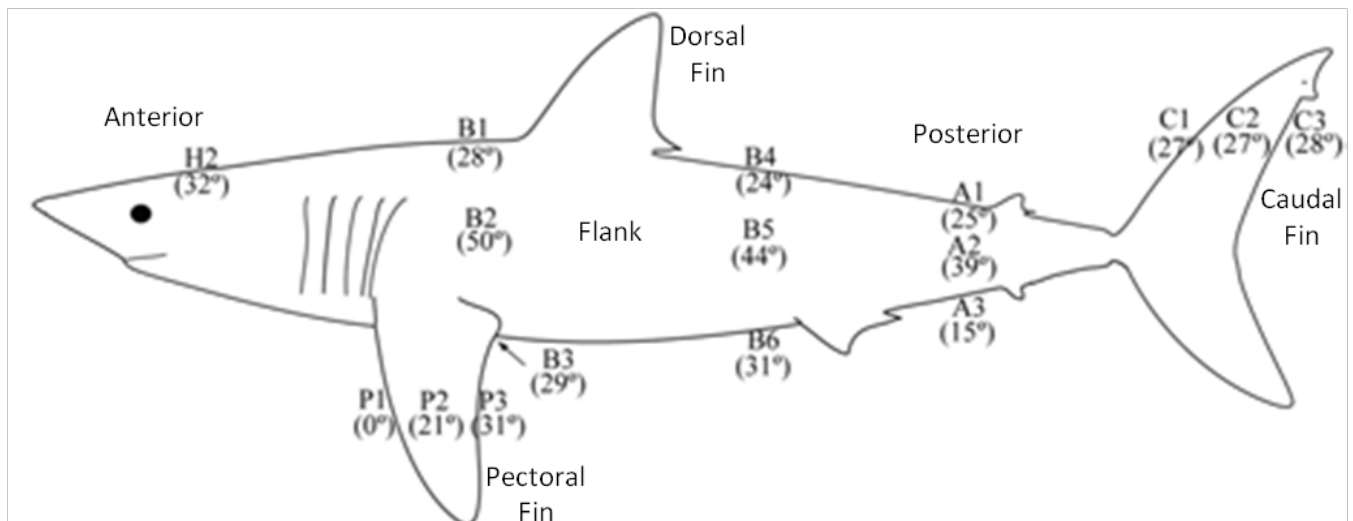


Figure 1.4 Diagram of measured scale bristling angles at various locations on the mako shark (Lang et al., 2011).

Bristling occurs when the scales are subjected to a shearing force in the posterior-to-anterior direction (opposite of the normal direction of flow), although the force required to erect a single scale has not been measured. Recent experiments have shown that the scales can be erected by reversed flow, such as would occur in the case of a separated boundary layer. When bristled, the pattern of the scales results in the creation of embedded cavities between scales in successive rows. It has been hypothesized that these embedded cavities formed by the bristled scales act as a means of passive, local separation control. When the boundary layer over a certain section of the shark's body begins to separate and low-momentum fluid is pushed upstream by the adverse pressure gradient, shear from the reversed flow causes the scales in that region to bristle and, as a result, this backflow becomes trapped in the cavities that form. These cavities impart a partial slip velocity on the boundary layer, which helps prevent the separated region of flow from progressing further upstream. This sort of local separation control would greatly aid the mako shark in being able to perform rapid changes in direction at high speeds, due to the resulting decrease in pressure drag. In addition, as a passive form of flow control, the bristling of the scales could increase the shark's swimming performance without any extra energy expenditure. This hypothesis agrees well with the work of Lang et al. (2011), which concluded that the mako shark has no means by which it could actively bristle its scales.

1.3 OBJECTIVE

The objective of this research was to compare the separation of turbulent flow over skin samples from a Shortfin Mako shark on a NACA 4412 hydrofoil model with that over the same model with a smooth surface. By mounting the skin on a hydrofoil, its flow characteristics could be seen on a curved surface in the presence of an adverse pressure gradient, which would be the conditions present on a mako shark's body at the location of the scales during a turning

maneuver. The NACA 4412 hydrofoil was chosen because of its trailing edge separation characteristics (Simpson, 1989). The experiments were run with the hydrofoil at angles of attack in the range of 8 to 16 degrees, all of which resulted in a region of separation occurring at some location over the top surface of the hydrofoil. In addition, the flow was tripped turbulent near the leading edge of the hydrofoil to better approximate the boundary layer conditions with those found over a shark's body, since the facility used in these experiments was incapable of matching the Reynolds number of a swimming shark (approximately 10^7 for the shark versus 10^5 for the tests). Two free stream speeds were used in the experiments in order to examine the effects of Reynolds number on the results. The flow measurements were primarily obtained using a time-resolved digital particle image velocimetry (TR-DPIV) system. All experiments were carried out in the University of Alabama's low-turbulence water tunnel facility.

These experimental conditions allowed for the comparison of flow over the two surfaces for several different cases with varying degrees of separation, from only moderate separation for the lowest angle of attack to post-stall conditions for the highest angle. The results were analyzed primarily by determining the backflow coefficient and average magnitude contours, as well as timelines of instantaneous velocity at specific points in the flow over the models. The backflow coefficient is defined as the percentage of time that flow is reversed, with respect to the total time over which a data set is recorded. The determination of this parameter gives a good indication of the size of the separated region over the hydrofoil, and also allows for the comparison of the results with the accepted definitions of the state of flow separation, namely, intermittent transitory detachment (20% backflow) and detachment (50%). Another backflow parameter, defined as the percentage of time that backflow with a magnitude greater than 10% of the free stream velocity was observed, was calculated to identify the frequency of the occurrence of high-

velocity reversed flow. Contours of average backflow magnitude were also generated to provide additional insight into the amount of momentum contained in the separated region over the total time that flow was reversed. The plotting of instantaneous point velocities versus time gave information about the frequency of changes in flow direction as well as the magnitude of peak negative velocities within each event of flow reversal. Boundary layer profiles were determined at locations where the boundary layer was of sufficient thickness to be resolved by the interrogation windows of the PIV processing software. Additional flow information such as overall velocity and Reynolds stress fields and turbulence intensity contours were also obtained to provide further insight into the differences between the two surfaces.

2. REVIEW OF LITERATURE

2.1 TURBULENT BOUNDARY LAYER SEPARATION

Much of the current understanding of the characteristics of turbulent boundary layer separation is a result of work summarized by Simpson (1996). These results showed that small three-dimensional elements of reversed flow can move up and downstream independently following regions of low kinetic energy, and that there is therefore no spanwise line of incipient detachment. It was also shown that the high turbulence energy in the separated flow near the wall is supplied by large turbulent structures, resulting in velocity fluctuations in the separated region which are often greater than the average backflow velocity, even when the free stream flow remains relatively steady. Intermittent backflow can occur at distances above the surface up to the point of maximum shear stress. Downstream of the point of detachment, the region of reversed flow is divided into three layers. Closest to the surface is a viscous layer dominated by turbulent unsteadiness which experiences little effect from shearing stresses. Next is an intermediate overlap layer with a semi-logarithmic time-averaged flow velocity profile. The outer layer of reversed flow is shown to be a part of the larger scale turbulence.

Simpson (1989) also investigated the effects of surface curvature on the separation of a turbulent boundary layer. He found that as a surface diverges downward from the local flow direction, the flow velocity near the wall must decrease more rapidly than it would for a flat surface experiencing the same pressure gradient, due to continuity requirements. As a result there is less Reynolds stress and turbulence energy diffusion available; and less momentum can be

transferred to the flow close to the wall. Therefore, the location of the point of flow detachment is farther upstream on a convex surface when compared to the location of detachment for a flat surface under the same flow conditions. This work also showed that there is a lag in the response of a separating turbulent flow to a diverging surface because the large-scale eddies containing much of the flow energy are unable to instantaneously respond to sudden changes in the boundary conditions. Due to the fact that the streamlines in the outer region of the turbulent boundary layer do not curve as rapidly as those located very close to the surface, a discontinuity in the boundary layer profile occurs and becomes more pronounced as the flow progresses downstream and the surface continues to fall away from the mean-flow streamlines.

The Reynolds-number dependency of turbulent boundary layer separation over a hydrofoil was studied by Bourgoyn et al. (2001). In these experiments, a modified NACA-16 hydrofoil was placed at zero degrees angle of attack in a high-speed water tunnel which generated Reynolds numbers on the order of 10^7 to 10^8 . LDV measurements of mean flow velocities and turbulence quantities near the trailing edge of the hydrofoil's upper surface showed significant variations in Reynolds stress profiles with the flow free stream speed at all locations observed. Additionally, the point of boundary layer detachment was found to move closer to the trailing edge as the Reynolds number increased for the zero-degree case, resulting in a separated region of decreasing size. At such high Reynolds numbers, the point of detachment occurred very close to the trailing edge for all speeds measured, with 50% flow reversal being achieved at $x/c > 0.985$.

Computational models of turbulent separation have also been investigated. Na and Moin (1998) performed a direct numerical simulation (DNS) of a separated turbulent boundary layer in a three-dimensional computational domain over a flat plate. Their method solved the governing

Navier-Stokes and continuity equations for incompressible flow on a staggered rectangular grid, integrated in time using a semi-implicit scheme. To generate the adverse pressure gradient needed for separation, they applied a suction-blowing velocity distribution along the top surface of the computational grid, which also resulted in a strong favorable pressure gradient at the location of reattachment. The results of this work showed that the shape of the instantaneous separation bubble changed significantly with time, and that the points of detachment and reattachment experience large changes in streamwise location even at low Reynolds numbers. This numerical simulation also showed that the spanwise profile of the detachment location was highly irregular and almost oscillatory in nature, indicating the existence of streak-like structures. However, the spanwise line of reattachment was shown to be smoother and experience much less fluctuation. The Reynolds stresses in the region of detached flow were found to be largest far away from the wall, and the pressure fluctuations in this region were greatly reduced when compared to those in the attached turbulent boundary layer.

Manhart and Friedrich (2002) later performed a direct numerical simulation of a separating turbulent boundary layer over a flat plate with a completely adverse pressure gradient over the region of the separation bubble to more closely match experimental conditions. This DNS also demonstrated significant spanwise fluctuations in the location of the detachment point, as well as the occurrence of large vortices reaching from the shear layer above the backflow region down to the wall, which result in a strong vertical momentum transport from the free shear layer. The length of the separation bubble was found to change with fluctuations in oncoming Reynolds stress values, indicating that the structure of the separation bubble is dependent on the level of turbulence energy in the upstream flow.

Badran (2003) performed a computational study of turbulent flow over a NACA 4412 airfoil, using two-equation turbulence models to predict the location of flow detachment on the upper surface of the airfoil at an angle of attack of 15 degrees. The results of this study found that the time-averaged point of detachment for the given case occurred at approximately $x/c = 0.7$ at a Reynolds number of 360,000, for all three turbulence models investigated. In addition, the skin friction coefficient and surface pressure values were found to agree well with previous experimental work.

2.2 PASSIVE SEPARATION CONTROL

A number of passive boundary layer separation control mechanisms have been investigated over the years. Passive flow control, normally achieved by altering the surface geometry over which the fluid is moving, is desirable because it requires no additional energy input to increase the aerodynamic or hydrodynamic performance of the surface in question. Perhaps the most widely used method of passive separation control is the employment of vortex generators on the surface of a wing. These are small, vertical protrusions into the boundary layer from the surface, typically arranged into v-shaped formations along a single spanwise line on a wing. As the flow encounters the vortex generators, streamwise vortices are created downstream, which add to the turbulent energy in the boundary layer. Lin (2002) performed a review of the use of low-profile vortex generators (those with a height of 10% to 50% of the boundary layer). The studies in this review showed a considerable increase in the aerodynamic performance (lift increase and drag decrease) of various airfoils at both low and high Reynolds numbers. Vortex generators were also shown to provide benefits in other applications, such as the reduction of interior noise in aircraft and the reduction of inlet distortion in ducts. This method of flow

control was found to be most effective on surfaces where the location of the point of separation remains relatively static.

Another method of passive separation control is the installation of movable spanwise flaps near the trailing edge of an airfoil, which was investigated by Bechert et al. (2000). This study found that when placed at a location on an airfoil of approximately $x/c = 0.9$, a freely-hinged flap resulted in a noticeable delay in the onset of stall. Furthermore, the implementation of a three-dimensional, jagged pattern on the trailing edge of the flap was shown to reduce drag in addition to increasing the airfoil's maximum lift value. As a result of this, it was hypothesized that three-dimensional separation over a wing could be effectively controlled if a movable flap were divided into separate, independently moving spanwise sections. Meyer et al. (2007) performed additional experiments on these flaps by varying the pressure downstream of the airfoil and observing the resulting movement of the flap. The results of this research showed no benefit in the use of active, oscillating flaps over freely-hinged passive ones, and also showed the same increase in lift for a movable flap activated by flow separation as was seen in the case of a static flap placed at an optimum angle.

Two-dimensional transverse grooves were first proposed as a possible means of separation control and skin friction drag reduction by Bushnell (1983), due to the generation of a partial-slip condition resulting from embedded vortices of trapped fluid in each groove. This was referred to as a 'micro-air bearing effect' because the embedded vortices were theorized to help the boundary layer 'roll over' the surface with less shearing stress than would be present in a no-slip condition. The reduction in shear stress and momentum loss in the boundary layer close to the wall could combat the effects of an adverse pressure gradient and delay the onset of separation. The results of experiments performed by Howard and Goodman (1985) agreed well

with this hypothesis, and showed a reduction in profile drag on an axisymmetric body. However, a study by Savill (1988) showed that, in the case of a turbulent boundary layer, the skin friction drag over a transverse-grooved surface was greater than that over a smooth surface, due to the additional motion of fluid into and out of the cavities.

Djenidi et al. (1999) performed an investigation on the effect of two-dimensional transverse square cavities on a turbulent boundary layer. This study employed Laser Induced Fluorescence visualization and Laser Doppler Velocimetry measurements to observe and analyze the exchange of fluid between the cavities and the boundary layer. Results showed that randomly occurring outflows from the cavities coincided with the passage of quasi-streamwise vortices in the near-wall region of flow. These outflows of low-momentum fluid added additional turbulence energy to the boundary layer and resulted in a significant increase in Reynolds stress when compared to the flow over a smooth surface. It was also found that the Reynolds stresses reached a maximum local value in the shear layer above each cavity, very near the location of the inflection point in the U average distribution. These results indicate that a surface pattern with transverse cavities is able to enhance the self-preservation of a turbulent boundary layer as compared to a standard smooth wall through added turbulent energy production and dissipation. However, the LDV measurements of this study show that even in the presence of the cavities, the turbulence of the boundary layer is not completely self-preserving.

2.3 FLOW CONTROL MECHANISMS OF SHARK SKIN

Much of the previous research on the hydrodynamic effects of shark skin has primarily focused on the ridges along the crowns of the scales, acting as riblets to reduce the skin friction drag over the shark's body. In these studies, the model scales were made to lie flat on the

surface, and the bristling of the scales was not investigated. Bechert et al. (2000) measured the drag present over a model of shark skin in a fully turbulent oil channel, allowing for some degree of bristling of the scales by attaching springs of varying tension to loosely anchored scales. This study found a 3% reduction in skin friction drag when the scales lay flat on the surface; however an increase in drag was noted in conditions where the scales bristled. It was also observed that regions of the model scale array would move up and down in reaction to localized pressure gradients. The scale models in these experiments did not achieve a bristling angle of greater than 12 degrees, and as a result the embedded vortex aspect of the scales' hydrodynamic performance was not analyzed. Instead, it was theorized that the bristled scales acted simply as vortex generators.

Recent work by Lang and Hidalgo (2009) analyzed the flow over a scaled-up shark skin model designed to match the Reynolds number of real shark skin at normal swimming speeds, based on the crown length of the scales (100x increase in crown length to achieve similarity with a 100x decrease in flow velocity). The scales in this model were fixed at a 90 degree angle to the surface to simulate a case of extreme bristling and focus primarily on the formation and effects of the embedded vortices in the cavities between the scales. In these experiments, the average velocity at the top of the scales (corresponding to $y=0$ on a flat surface) was shown through time-resolved PIV measurements to be approximately 14% of the free stream velocity, confirming the existence of a partial slip condition over the model. In the case of a fully turbulent boundary layer, the Reynolds stress at the top of the cavities between the rows of scales was observed to increase with streamwise distance, indicating an enhanced mixing of the low momentum fluid in the cavities with the high momentum fluid in the boundary layer. This study also displayed the formation of both primary and secondary vortices in the cavities between scales, as well as a

higher degree of flow symmetry in the low-momentum flow close to the wall than was seen over two-dimensional grooved models in the same study. It was therefore hypothesized that the combination of the three-dimensional geometry of the scales and their orientation when bristled could lead to a reduction in 3D boundary layer separation over the surface to which the scales are applied.

Tests were conducted by Lang et al. (2011) on the scales of various shark species in order to determine the maximum bristling angle of the scales while still maintaining their structural integrity within the skin. The skin of a great hammerhead (*Sphyrna mokarran*) was pressurized to 14 psi by a catheter placed under the skin and was observed to bristle slightly. Preliminary tests on both the great hammerhead and a blacktip shark (*Carcharhinus limbatus*) showed that the scales could be manually manipulated to a bristling angle of greater than 30 degrees above the skin surface, significantly higher than what had been tested before. Of particular importance to this research, samples of skin from shortfin mako (*Isurus oxyrinchus*) specimens were removed and affixed to plexiglass plates so that the scales could be manually bristled and their relaxed position observed. It was determined that the scales present on samples from the flank region of the shortfin mako could be bristled to angles of approximately 50 degrees, and that the scales would hold this angle as the skin sample dried. Skin samples from many locations on the shark's body were collected and measured, showing a general trend of increasing maximum bristling angles as the skin's distance from the anterior end of the shark increased, up until just beyond the point of maximum body thickness, after which the flexibility of the scales was measured to decrease slightly. Scales on the head of the shark and on the leading edges of its fins were found to be nearly rigid. Scales along the top of the shark's body were also found to achieve a lower bristling angle than those located along its centerline. The flank regions of the

shark exhibited the highest scale bristling angles in all cases. SEM images of individual scales (Figure 2.x) showed that the most flexible scales from the flank region had wide, short bases, while the less flexible scales located in other regions had bases which were more uniform in shape. The results of these tests were the primary reasoning behind the selection of the skin samples used in the present research.

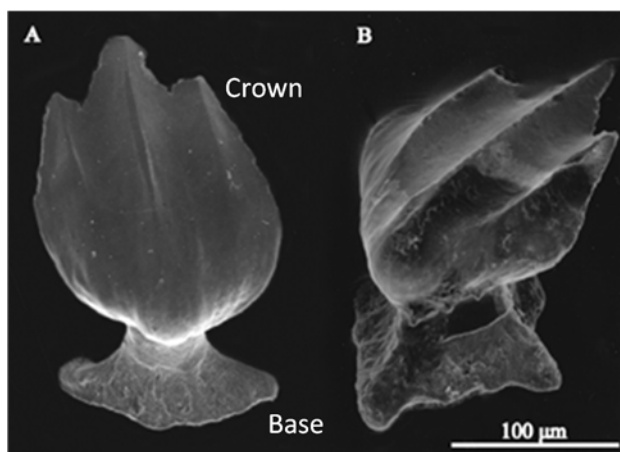


Figure 1.4 SEM of individual scales; highly flexible scale from flank region (A) and less flexible scale from dorsal region (B) (Lang et al., 2011).

3. EXPERIMENTAL SETUP

3.1 EXPERIMENTAL FACILITY

The experiments for this research were conducted in the University of Alabama's water tunnel facility. The water tunnel was manufactured by Rolling Hills Research Corporation as a modified version of the Eidetics Model 1520 tunnel. This custom-built model, designated 1520-EXT, employs a test section with a length of 108 inches and a height of 30 inches. To account for the growth of the boundary layer displacement thickness along the length of the test section, the width of the tunnel increases from 16.25 inches at the beginning of the test section to 17.25 inches at the end of the test section. The total volume of the standard Model 1520 tunnel is approximately 1000 gallons; the capacity of the University of Alabama's model is slightly higher due to the extended test section (108 inches versus 60 inches). Maximum free stream velocity of the standard tunnel is rated at 1.0 ft/s, but with the installation of a high-performance impeller and the reduction of the tunnel water level, the UA tunnel is capable of free stream speeds of over 1.64 ft/s (0.5 m/s) in the test section. The impeller is driven by a 2.0 horsepower, 230 V, 3-phase electric motor with a frequency range of 0-60 Hz.

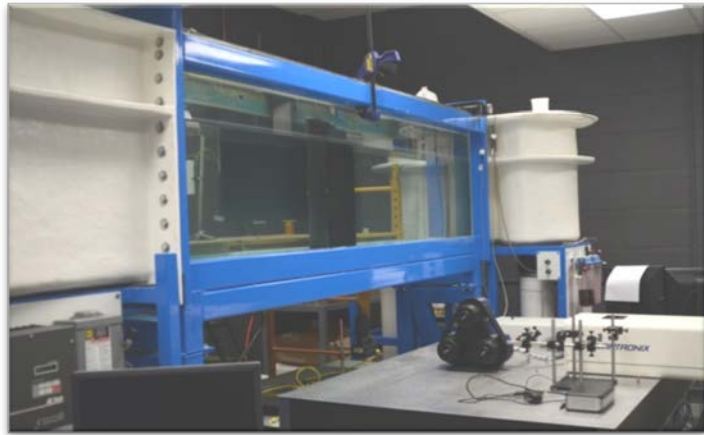


Figure 3.1 University of Alabama water tunnel facility.

An additional design modification of the Model 1520-EXT is the installation of two additional stainless steel baffles within the inlet plenum in order to improve flow distribution and reduce free stream turbulence. To further reduce flow turbulence, two porous plates and three stainless steel screens are positioned immediately following the honeycomb flow straightener located between the inlet plenum and the test section. According to tests conducted by the manufacturer, these modifications result in an average turbulence intensity of 0.41% at a test section free stream velocity of 2.0 in/s. To ensure this low turbulence intensity, the water tunnel must be cleaned and re-filled with fresh water regularly, as any particles that become trapped in the screens or honeycomb straightener could potentially affect the quality of the flow.

3.2 Experimental Model

The NACA 4412 hydrofoil model used in these experiments was cut from a 2-inch thick sheet of clear plexiglass by inputting the hydrofoil coordinates into a precision CNC machine. The hydrofoil section measured 610 mm (24 inches) span by 305 mm (12 inches) chord. To hold the model securely in place in the water tunnel, it was attached to a mounting bracket composed

of aluminum and stainless steel plates. The stainless steel portion of the mounting bracket rested on the submerged bottom surface of the tunnel, and the top aluminum plate was clamped to the top of both the front and back walls of the tunnel. The airfoil model was placed vertically in the tunnel and connected to the mounting bracket by a steel rod at the top and a bushing at the bottom, allowing it to rotate freely until locked in place by the angle of attack dial (see Figure 3.2). Tick marks were etched into the top aluminum plate so that the airfoil could be set at any angle of attack from -90 degrees to +90 degrees in increments of one degree, the zero-degree mark being aligned with the centerline of the water tunnel test section. The mounting system positioned the chord line of the hydrofoil at the midpoint of the tunnel width in order to maximize the distance between the hydrofoil surface and the tunnel walls. The bushing at the bottom edge of the mounting system was made as thin as possible so that the three-dimensional flow generated around this edge could be reduced. All fabrication of this experimental model was completed by the University of Alabama engineering machine shop.

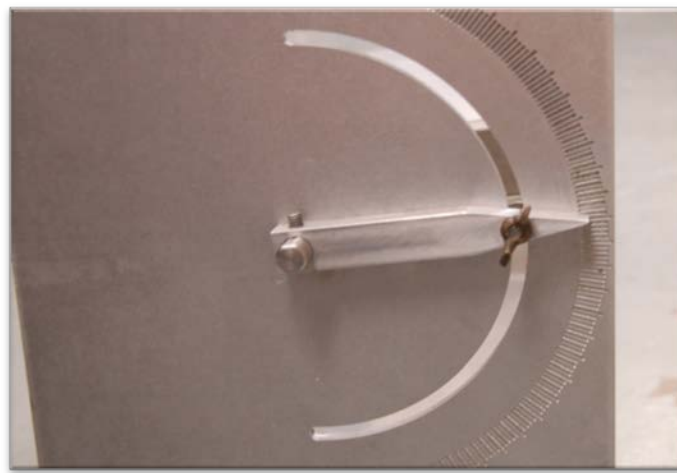


Figure 3.2 Angle of attack selection dial on top of hydrofoil pivot plate.

Two identical models were fabricated according to these specifications, so that the painted surface and shark skin experiments could be run independently on separate models. The smooth surface model was painted using standard matte black spray paint to minimize reflections from the PIV laser sheet (see Figure 3.3). It was then sanded to eliminate the grain present in the paint and ensure the smoothness of the surface. The hydrofoil model used with the shark skin samples was not painted since the laser sheet would only come into contact with the surface overlaid with the samples. The flow over the upper surface of both models was tripped by a 2mm-diameter copper tube placed at the 5% chord location across the entire span of the hydrofoil.



Figure 3.3 Painted NACA 4412 hydrofoil and mounting system, view from bottom.

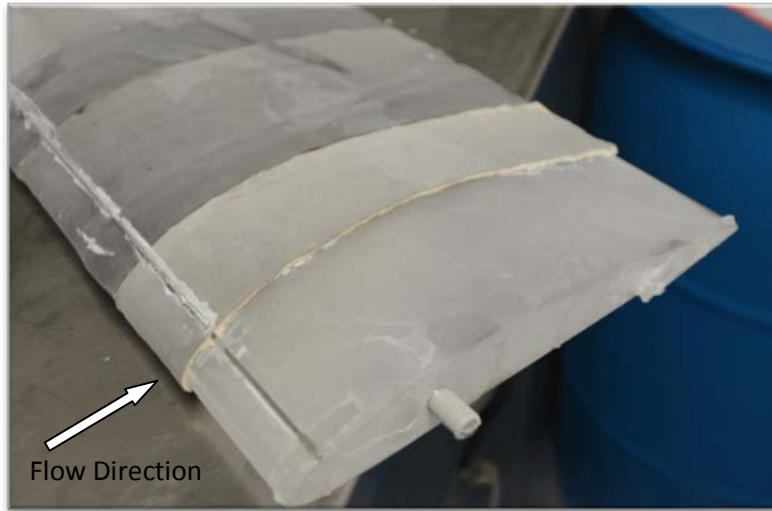


Figure 3.4 NACA 4412 hydrofoil with affixed shark skin samples, frozen.

The skin samples used on the second model were three rectangular flank sections, two with dimensions of 3"W X 13"L and one measuring 6"W X 13"L. The wider section was placed on the model so that its centerline coincided with the mid-depth spanwise location of the hydrofoil. The two thinner sections were placed adjacent to this section on either side, so that a total of 12 inches of span on the hydrofoil was covered with skin samples (Figure 3.4). The samples were attached to the surface, starting at the leading edge, using successive rows of super glue to ensure the skin lay flat on the hydrofoil surface. Some skin was allowed to overlap the leading edge so that the blunt edge of the skin sample did not obstruct the flow at the front of the hydrofoil.

It should be noted that, while every effort was made to cut the skin samples to the exact dimensions given above, some imperfections remained in the shape of the samples, particularly at the trailing edge. This was due to the orientation of fibers within the lower layer of the skin that prevented a perfectly clean cut with a surgical blade. Further cuts were not attempted

because of concern for destroying much larger sections of the skin samples. These irregularities are shown in Figure 3.5.

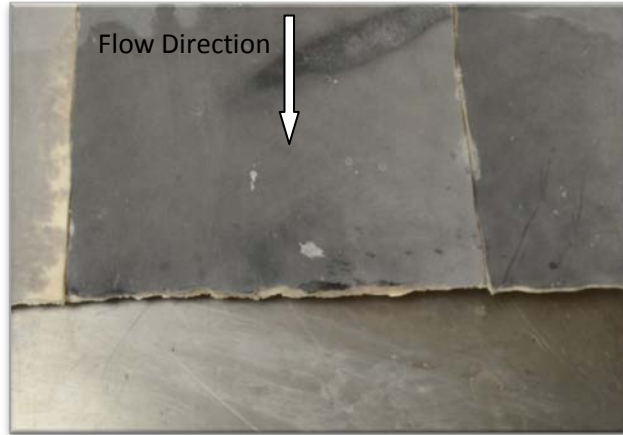


Figure 3.5 Trailing edge of center shark skin sample.

Due to the fact that any biological material deteriorates quickly when exposed to air at room temperatures, the hydrofoil model with the skin samples was stored in a freezer when it was not in use. The skin was allowed to thaw for approximately 30 minutes before being placed in the water tunnel, and returned to the freezer promptly after the experiments had been run. Based on information supplied by University of South Florida biologists, the skin samples could be thawed and refrozen approximately five times before damage to the scales would begin to occur. In the event that experiments were run on two consecutive days, the model was placed in a large cooler filled with an ice/water mixture so that the skin could be preserved without being completely refrozen. Care was also taken so that the surface of the samples did not come into contact with any other surface or object, as doing so would likely destroy patches of scales on the skin.

3.3 DPIV SYSTEM

A time-resolved digital particle image velocimetry system was used as the primary method of flow measurement in this research. The system consisted of a pulsed solid-state laser, a high speed digital camera, image acquisition software, and PIV processing software. The particles used to seed the water tunnel for these PIV measurements were silver-coated hollow glass spheres with an average diameter of 14 μm , manufactured by Potters Industries, Inc. These particles are neutrally buoyant in water and are the optimum size for the processing windows used in the PIV processing software.

The laser used was a Falcon 30 series Nd:YLF system manufactured by Quantronix Corporation. This laser generates a beam with a wavelength of 532 nm and a maximum power output of 20 watts, with a current range of 7 to 30 amps. The Falcon laser is water-cooled with an external power supply unit and chiller, which keeps the laser head at an operating temperature between 27°C and 32°C. It can be pulsed at a frequency in the range of 0.1 to 1.0 kHz; all of the experiments in this research were run with the laser pulsed at either 400 or 500 Hz, depending on free stream speed. After being emitted from the laser housing, the output beam was re-directed to the measurement plane of the water tunnel and reduced in diameter by 60% by a set of lenses, the first lens with a focal length of 100 mm and the second with a focal length of 40 mm. The beam was then spread into a triangular sheet by a concave lens to create an illuminated plane for image acquisition. The mirror and lenses were mounted on an elevated, adjustable-height optical board so that the vertical location of the laser sheet could be easily changed. A diagram of the experimental setup is shown in Figure 3.6.

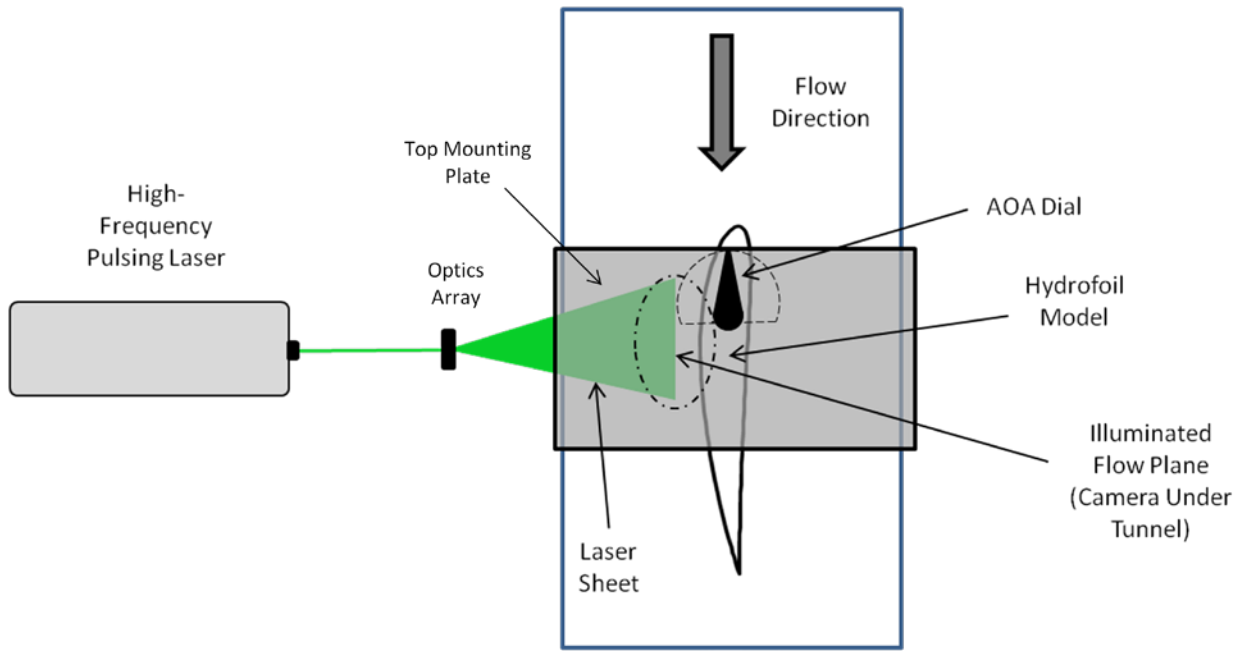


Figure 3.6 Top-down diagram of experimental setup in water tunnel test section. Camera is located under the test section directly below the measurement plane.

The camera used to record the raw PIV images was a Basler A504k 8-bit high-speed digital camera with a Nikon AF Micro Nikkor 105mm lens. This camera was capable of acquiring images with a resolution of 1280x1024 pixels at a frame rate of up to 500 frames per second. Higher frame rates could be achieved by reducing the camera's resolution. For all runs in these experiments, the camera frame rate was matched with the laser pulse rate, and the full resolution of the camera was used. Due to the high pulse frequency of the laser and the exposure time of each image, a synchronizer was unnecessary for generating consistent images. Though the Nikkor lens had auto-focus capabilities, the camera was manually focused on the illuminated plane of the laser sheet to ensure consistent sharpness of the particles and surfaces between experiment runs. The camera was linked to a PC by a National Instruments PCIe-1429 frame grabber, which worked in conjunction with a LabView program to capture and store the images on the computer in TIFF format. Each run of image acquisition saved 1200 images, and four runs

were taken for each combination of experimental conditions (angle of attack, free stream speed, location on hydrofoil) for a total of 4800 images per case. The number of images per capture was chosen to be 1200 because of previous experience with the system, where higher numbers of images per run resulted in program instability and frequent software crashes. After capture, the images were converted into sequential, overlapping pairs by another LabView program. In this method of pairing, Images 1 and 2 were saved as Images 1A and 1B, Images 2 and 3 were saved as Images 2A and 2B, and so on. This resulted in the same number of overlapping pairs as original raw images; these pairs could then be imported into the PIV processing software.



Figure 3.7 Basler high-speed camera (left) and Quantronix pulsed laser (right).

PIV processing and preliminary analysis was performed through use of Insight 3G, a PIV software program developed by TSI, Incorporated. This program takes the aforementioned TIFF-format image pairs as input and computes the resulting vector field for each pair in the 1200-image run being processed, given the change in time between the first and second image in the pair. The length scale calibration of the images must also be input into the program. This was determined by placing a ruler in the illuminated measurement plane of the flow and capturing a test image, then measuring the distance in pixels between the centimeter tick marks on the ruler in the image. The Insight software breaks the images into a grid of interrogation windows and

can be run in multiple passes with progressively smaller window sizes for increased resolution, down to a minimum window size of 8x8 pixels. It uses an FFT correlator between corresponding interrogation window pairs and allows for a maximum particle displacement of 25-49% of the window width between the first and second images. A mask can be applied to the processing window to prevent the software from attempting to process regions below a surface, or near the edges of the laser sheet where the illumination is insufficient for good seeding particle definition. The program provides a number of pre- and post-processing applications, such as image background removal, local and global vector validation, and vector interpolation. For this set of experiments, no pre-processor was employed, and a post-processor containing local vector validation and vector interpolation was used to remove any bad vectors generated by the processor and fill any gaps based on the values of surrounding vectors.

The Insight 3G software also provides a MATLAB add-on for basic plotting of results. Velocity values such as u, v, and velocity magnitude can be graphed for both instantaneous and averaged vector fields. Flow fluctuation information such as Reynolds shear stress, u and v turbulence intensities, and root-mean-square velocity fluctuations can be plotted for average vector fields. In addition, velocity, vorticity, and Reynolds stress profiles can be displayed for individual columns of vectors at any location in the flow field.

3.4 EXPERIMENTAL PROCEDURE

In order to provide a range of results by which to compare the flow over the two surfaces in question, PIV measurements were taken at multiple combinations of angle of attack, free stream speeds, and chordwise locations on the hydrofoil. The measurement locations were laid out such that the flow field over the entire chord length of the upper surface of the hydrofoil

could be analyzed, with some overlap in the locations starting at 50% chord length. For the primary set of experiments, the illuminated plane of the laser sheet was set at mid-depth of the water tunnel test section, and the vertical position of the camera below the water tunnel was adjusted accordingly to produce the correct width of each image location. A total of 5 measurement regions were used to cover the length of the model; the upstream edge of each window location was aligned with the point corresponding to 0, 25, 50, 66.7, and 83.3 percent chord (0, 3, 6, 8, and 10 inches from the leading edge), respectively (Table 3.1). A field of view of approximately 7 cm was used at each measurement window location. The first and second measurement locations were aligned with the x- and y-coordinates of the centerline of the water tunnel, while the last three locations were aligned with the local coordinates of the hydrofoil surface, due to the lower curvature at these locations. These same five locations were used for all combinations of angle of attack and free stream speed. A diagram of the orientation of these measurement regions is shown in Figure 3.8.

Window Number	Starting Position (x/c)
1	0.000
2	0.250
3	0.500
4	0.667
5	0.833

Table 3.1 Starting positions of measurement window locations.

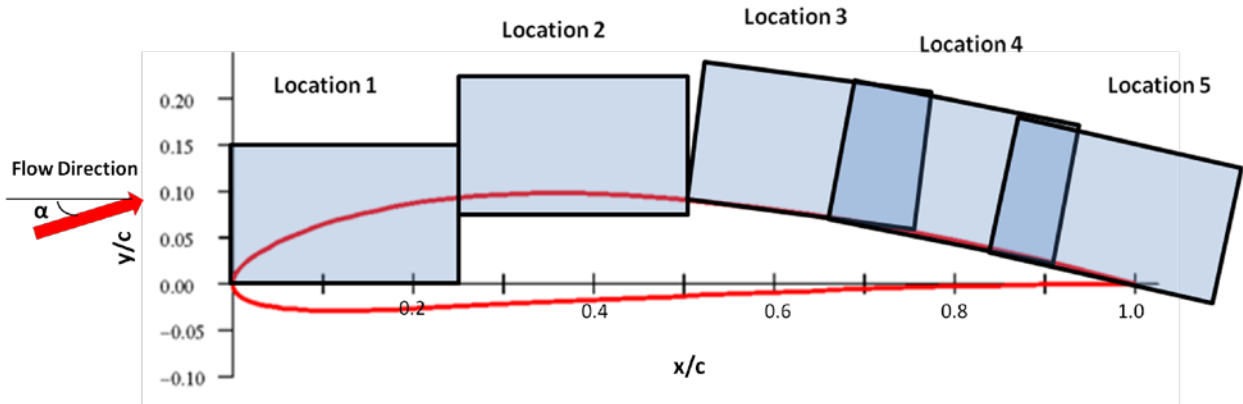


Figure 3.8 Diagram of measurement window locations and orientations.

The angles of attack tested in these experiments were 8, 10, 12, and 16 degrees. The top mounting bracket for the hydrofoil model had to be aligned carefully with the edge of the water tunnel walls to ensure that the angle of the hydrofoil was the true angle of attack with respect to the free stream. The two test section free stream speeds used were 32 and 50 centimeters per second, resulting in chord-length Reynolds numbers of approximately 100,000 and 152,000. These speeds corresponded to pump motor frequencies of 40 and 60 Hz, which were set through the water tunnel's drive control panel. A calibration chart was generated to correlate the free stream speed and motor frequency; for this calibration to be valid, the water depth in the tunnel had to be set to the same level each time the tunnel was re-filled. The calibration was performed by taking PIV measurements of an arbitrary plane in the water tunnel with no model installed, then calibrating the length scale of the images and determining the resulting unobstructed free stream velocity.

The combination of 5 measurement windows, 4 angles of attack, and 2 free stream speeds resulted in 40 unique cases being run for each surface configuration, with four separate runs taken for each case. In order to minimize the movement and adjustment of the laser and optics,

all runs for a given angle of attack and image location were completed consecutively. The angle of attack of the hydrofoil was then changed and the orientation of the camera was adjusted as needed; this procedure was repeated for all angles of attack at a given image location. Once these runs were completed, the entire hydrofoil model and mounting system was moved forward so that the illuminated plane of the laser sheet would coincide with the next measurement location, and the process was repeated. Each time the free stream speed was changed from 32 cm/s to 50 cm/s, the frame rate of the camera and the pulse rate of the laser were changed from 400 Hz to 500 Hz to account for the increased displacement of the seeding particles due to the higher flow speed.

After the runs for all cases had been taken and the images converted into consecutive pairs, each run was loaded into the Insight 3G software individually for processing. A separate processing mask was applied at each measurement location to block out the regions of the image below the hydrofoil surface. For all cases run at a free stream speed of 32 cm/s, the processor within Insight was set to use a recursive Nyquist grid with an initial interrogation window size of 128x64 pixels and a final window size of 32x16 pixels. A rectangular grid was used in order to improve the resolution in the y-direction while still allowing for high x-direction displacement. The maximum particle displacement was set to 30% of the interrogation window width, and the change in time for vector calculation was set to 2500 μ s. For cases with a free stream speed of 50 cm/s, a recursive grid with the same initial window size was used, but with a final window size of 64x16 pixels due to the greater speed of the seeding particles. In these higher speed cases, the maximum displacement was set to 40% of the window width, and the vector delta t was changed to 2000 μ s.

It should be noted that for all cases run with the shark skin model, the measurement plane had to be lowered approximately 3 cm below the mid-depth position used for the painted surface model. This was due to two ridges in the 6-inch wide middle skin sample which ran the entire chord length of the model, and cast a shadow on the measurement region if the laser sheet was placed above it. These ridges were caused by a tendon beneath the skin and could not be removed without sacrificing the integrity of the sample. For this reason, the laser sheet was lowered to a depth just below the ridges and the measurements were taken at this location. An image of the skin sample showing these ridges is shown below in Figure 3.9.

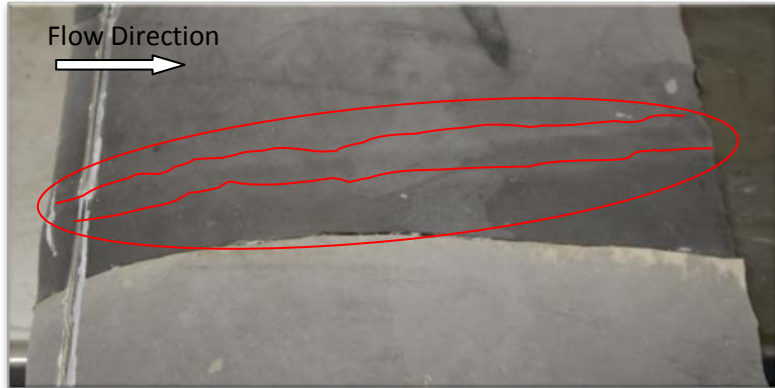


Figure 3.9 Ridges present on center-depth skin sample are circled in this image.

Once preliminary results showed that the collected data could be significantly affected by three-dimensional flow caused by the free surface interaction at the top of the water tunnel, an additional set of experiments at key locations and angles of attack was run with the measurement plane located at 75% depth in the water along the span of the hydrofoil. These runs were taken for both surface configurations at angles of attack of 10 and 12 degrees with a measurement window in the region of the trailing edge. Both free stream speeds were used, and four 1200-image runs were again taken for each case. A new calibration was performed to account for the

decrease in distance between the measurement plane and the camera. The same processor settings were used in these runs as were used in the primary experiment set. The length scale calibrations and resulting fields of view are listed in Table 3.1.

Painted Surface		
Application	Length Scale Calibration ($\mu\text{m}/\text{pix}$)	Field of View (mm)
50% Depth Locations 1-4	57.31	73.36 x 58.66
50% Depth Location 5	55.95	71.62 x 57.29
75% Depth	39.26	50.25 x 40.20
Shark Skin		
Application	Length Scale Calibration ($\mu\text{m}/\text{pix}$)	Field of View (mm)
50% Depth Locations 1-5	55.73	71.33 x 57.07
75% Depth	39.26	50.25 x 40.20

Table 3.2 List of digital length scale calibration values and fields of view for all measurement windows used.

In several key cases, the raw images recorded by the camera were used to generate videos of the flow to provide a more qualitative, easy-to-visualize representation of the separated region over the hydrofoil. For each case, the images were loaded into Windows Movie Maker and saved as a .wmv file. The brightness of the images was increased so the movement of the particles could be more easily seen, and the playback frame rate was set to 10 frames per second. Videos were generated for the runs of each angle of attack at the locations where separation was observed to occur; a list of these videos is given below.

An attempt was made to obtain PIV data in a plane parallel to the top surface of the hydrofoil, in order to better document the spanwise changes in the flow field due to three-dimensional effects. In this experiment, the laser optics were arranged so that the laser sheet would come up from underneath the water tunnel and coincide with the xz-plane of the hydrofoil, approximately 5 mm above its surface. The camera was positioned to the side of the

water tunnel test section with the lens focused on the laser sheet. Because the hydrofoil model was placed at an angle of attack, the camera had to be rotated to the same angle as the surface of the hydrofoil so that the lens face was parallel with the illuminated measurement plane. However, this also required that the camera be at an angle to the side wall of the water tunnel, which caused the refraction angle between the glass surface and the water to change along the width of the images being captured. This resulted in the camera only being able to focus on a partial region of the image, blurring the edges on both sides. The processing software was unable to correctly identify the blurred seeding particles, and as a result, these images could only be used for flow visualization videos. The field of view of these images was approximately 5 cm, with one run being centered on the 50% depth location on the hydrofoil surface, and another centered at 75% depth.

4. RESULTS AND DISCUSSION

4.1 MEAN VELOCITY FIELD

The mean velocity field for each case in the experiment was generated as the average of all 4800 instantaneous velocity fields in that case. While much of the turbulent fluctuation of the flow cannot be seen in averaged flow fields such as these, the velocity contour plots still provide useful information such as the maximum edge velocity (due to the curvature of the hydrofoil's upper surface) in each case at each measurement location and a visualization of the deceleration of the flow over the hydrofoil model due to the adverse pressure gradient. The measurement location observing the trailing edge of the model (Location 5) was investigated first due to the fact that turbulent separation begins close to the trailing edge and moves forward as angle of attack increases. The results for the cases run at $Re=100,000$ are discussed here.

Little difference was seen between the mean velocity fields of the two different surface configurations at the three lower angles of attack. For $\alpha=8^\circ$, the edge velocity at the top of the measurement region was observed to slow from nearly 70 cm/s at $x/c = 0.1$ to approximately 35 cm/s at the trailing edge for both the smooth painted surface and the shark skin surface. The deceleration of the flow was nearly the same for both surfaces, demonstrating the presence of similar adverse pressure gradients between the surface geometries. Comparable results were seen for the cases run at $\alpha=10^\circ$ and $\alpha=12^\circ$. At $\alpha=16^\circ$, a slightly higher edge velocity was maintained at the trailing edge for the shark skin surface, and the region of very low-speed flow (less than 0.5 cm/s) was observed to extend above the surface a considerably shorter distance than in the

case of the painted surface. A mean velocity of 0.5 cm/s was reached at a height above the trailing edge of approximately 8mm for the shark skin surface, whereas this velocity was not reached until a height of 30mm above the trailing edge of the painted surface. The velocity fields for both surfaces in this case are displayed in Figure 4.1. These results seem to show that at a Reynolds number of 100,000, the shark skin surface has an insignificant effect on the time-averaged velocity field in most cases.

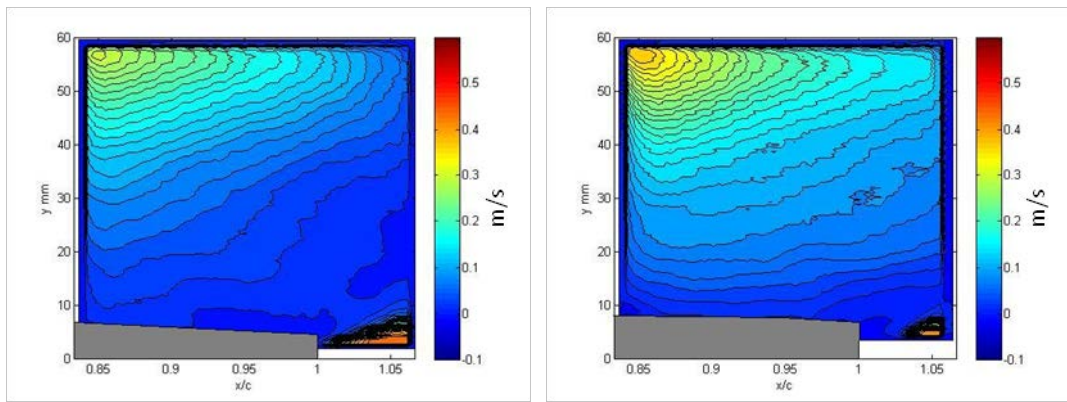


Figure 4.1 Mean velocity field, $Re=100,000$, $\alpha=16^\circ$, Location 5. Painted (left) vs. shark skin (right).

4.2 BACKFLOW COEFFICIENT

Backflow coefficient contour graphs were generated in MATLAB for all cases where regions of backflow occurred at least 10% of the total run time at some point in the measurement location for that respective case. These measurement locations are given in Table 4.2. Backflow coefficient contours were created for both individual 1200-image runs and for each overall 4-run case. To ensure that regions of invalid vectors in instantaneous images did not affect the outcome of the backflow calculation, each vector in each image was checked for validity before being added to the total number of vectors for its respective location in the processing grid. From these contours, the locations on the hydrofoil surface corresponding to intermittent transitory

detachment (20% backflow) and detachment (50% backflow), as well as the height of the lowest backflow coefficient line (10%) at key chordwise locations, could be determined and are displayed below in Table 4.1. The results for $Re=100,000$, averaged over 4800 images, at all four angles of attack are given here.

Painted Surface					
AoA	Location of ITD (x/c)	Location of D (x/c)	$h_{sr}, x/c = 0.75$ (mm)	$h_{sr}, x/c = 0.9$ (mm)	$h_{sr}, x/c = 1.0$ (mm)
8°	0.974	-	-	-	6
10°	0.912	-	-	4	8
12°	0.865	0.941	-	10	20
16°	0.638	0.719	27	36	50
Shark Skin Surface					
AoA	Location of ITD (x/c)	Location of D (x/c)	$h_{sr}, x/c = 0.75$ (mm)	$h_{sr}, x/c = 0.9$ (mm)	$h_{sr}, x/c = 1.0$ (mm)
8°	0.948	-	-	4	6.5
10°	0.875	0.983	-	7	8
12°	0.798	0.882	-	14	20
16°	0.651	0.795	10	18	28

Table 4.1 $Re=100,000$ results for chordwise location of ITD and D, and height above the surface of the 10% backflow contour line.

AoA	Re=100,000	Re=152,000
8°	Location 5	Locations 4,5
10°	Locations 4,5	Locations 4,5
12°	Locations 4,5	Locations 3,4,5
16°	Locations 3,4,5	Locations 2,3,4,5

Table 4.2 List of measurement window locations where at least 10% backflow was observed.

At an angle of attack of 8 degrees, the region of reversed flow did not begin until very close to the trailing edge for both surface configurations. The first backflow coefficient contour line (10% backflow) originated at a point approximately 18 mm ahead of the trailing edge on the

painted surface and 25 mm ahead of the trailing edge for the shark skin surface. The point of ITD occurred 16 mm in front of the trailing edge on the shark skin surface and 8 mm ahead of the TE on the painted surface. Detachment (50% backflow) was not reached on either surface at this angle of attack, although higher backflow percentages were seen in the wake. The maximum height of the region of backflow at the trailing edge was approximately the same for both surfaces, on the order of 6-7 mm above the surface. Contour plots of the backflow coefficient at Location 5 showing the results described above are displayed below in Figure 4.2.

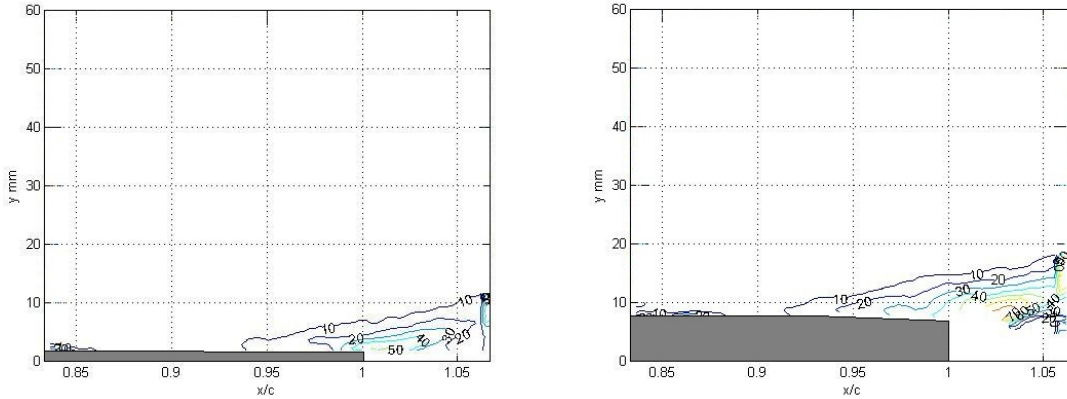


Figure 4.2 Backflow coefficient contours, $Re=100,000$, $\alpha=8^\circ$, Location 5. Painted surface (left) vs. shark skin (right).

For the case of $\alpha=10^\circ$, the length of the backflow region grew considerably on both surfaces, such that backflow contour lines were seen over the entire surface at Location 5. The point of ITD was seen 38 mm ahead of the trailing edge ($x/c = 0.875$) on the shark skin surface and 25 mm ahead of the trailing edge ($x/c = 0.912$) on the painted surface. 50% backflow was only observed in the wake of the painted surface model, however in the case of the shark skin surface a region of 50% backflow began at $x/c=0.983$. Although the length of the backflow region increased significantly from the $\alpha=8^\circ$, the height of the first backflow contour line above

the trailing remained nearly the same, approximately 8 mm for both surface configurations.

Backflow was seen at the Location 4 measurement region as well for the shark skin surface, with the 10% contour line originating at $x/c=0.788$. The backflow contours of Location 5 are shown in Figure 4.3.

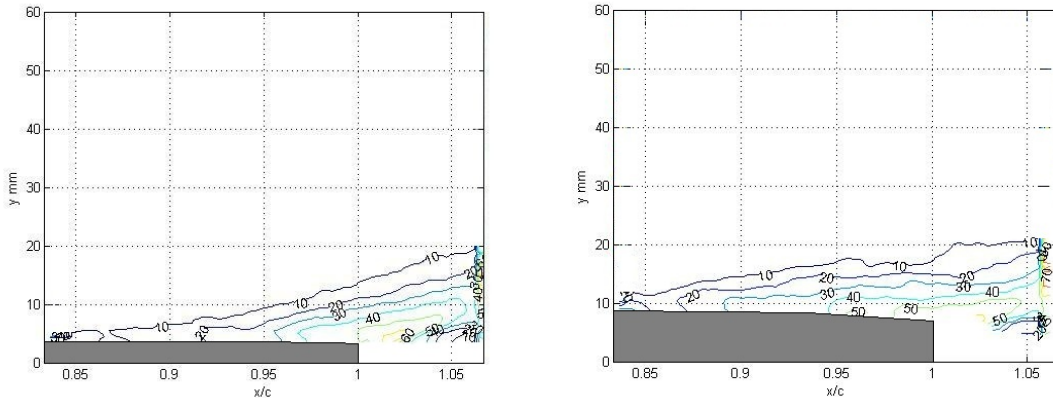


Figure 4.3 Backflow coefficient contours, $Re=100,000$, $\alpha=10^\circ$, Location 5. Painted surface (left) vs. shark skin (right).

When the angle of attack was increased to 12 degrees, a general increase in the thickness of the separated region was observed, and backflow was seen to occur a greater percentage of the time. Very near the trailing edge, regions of 70-80% backflow were seen close to the surface for both configurations. The point of detachment was observed to occur at an earlier location on the shark skin surface than on the painted surface, $x/c=0.882$ compared to $x/c=0.941$. Regions of higher backflow (60% and above) were considerably more prominent over the shark skin surface compared to the painted surface. The maximum thickness of the backflow region was approximately 20mm above the surface for both configurations, more than twice what had been observed for the lower angles of attack.

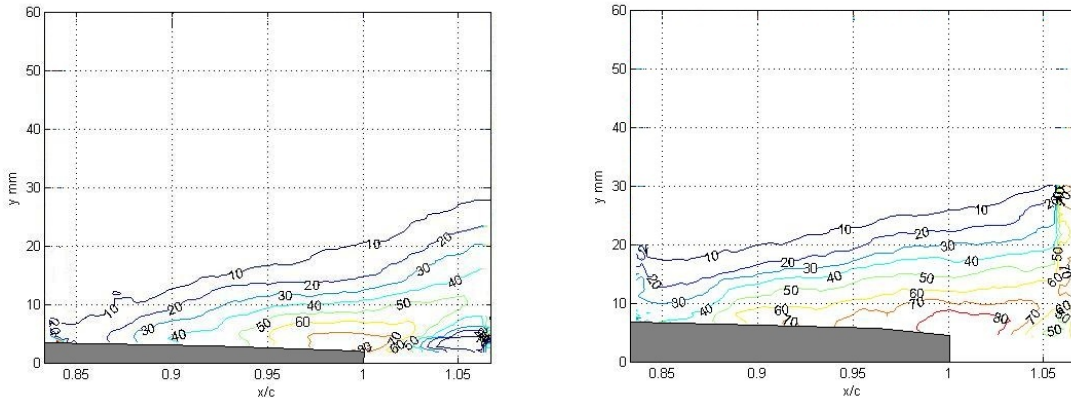


Figure 4.4 Backflow coefficient contours, $Re=100,000$, $\alpha=12^\circ$, Location 5. Painted surface (left) vs. shark skin (right).

The size of the separated region was observed to become much greater at $\alpha=16^\circ$, spanning measurement locations 3, 4, and 5. However, the previous trend of more upstream locations of ITD and detachment for the shark skin surface were reversed for this angle of attack. The point of 50% backflow was measured approximately 26 mm further downstream on the shark skin surface than on the painted surface. For both surface configurations, a "bubble" of 50% or higher backflow was observed to occur, unlike the lower angles of attack where the 50% backflow regions were continuous to the trailing edge once detachment had been achieved. Within this bubble, backflow coefficient values of 80% were seen in the case of the painted surface, however no higher than 60% backflow was measured above the shark skin. A second region of 50% backflow was seen to extend into the wake over both surfaces, although this second region was considerably smaller in the case of the shark skin surface. The height of the backflow region was also considerably less for the shark skin surface across all three measurement windows. At $x/c=0.75$, the height of the 10% backflow line was approximately 10 mm above the shark skin surface, compared to a height of 27 mm for the painted surface at the same location. This trend continued to the trailing edge, where the height of the backflow region

was measured to have a height of 28 mm on the shark skin surface and a height of 50 mm on the painted surface. The contour plots for the separated region for both surfaces at $\alpha=16^\circ$ are shown below in Figure 4.5.

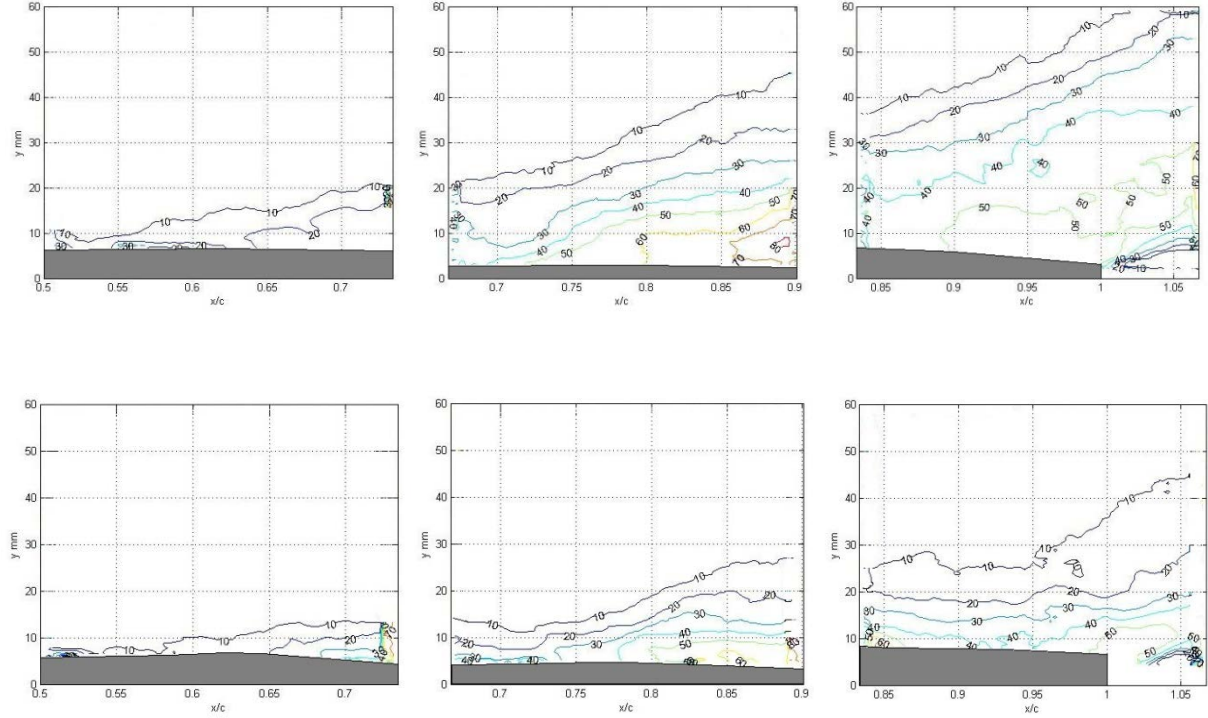


Figure 4.5 Backflow coefficient contours, $Re=100,000$, $\alpha=16^\circ$, Locations 3-5. Painted surface (top) vs. shark skin (bottom).

4.3 10 PERCENT FREE STREAM BACKFLOW

An additional backflow parameter was used to quantify the percentage of time that higher magnitude backflow was present over the two surfaces. These plots display contours corresponding to the percentage of valid velocity vectors which were measured to have a value of at least 10% of the free stream velocity, in the reverse direction. The plots shown below are each averaged over all 4800 images from their respective runs. The results from the $Re=100,000$ case are discussed here.

At 8 degrees angle of attack, the backflow reaches a magnitude of 10% free stream (3.27 cm/s) only a very small percentage of the time over either surface, and only in a region very close to the trailing edge. Contour lines representing the backflow reaching this magnitude 10% of the time or greater are only seen in the wake of the shark skin surface, and not at all in the case of the painted surface. For the runs at $\alpha=10^\circ$, 10% free stream reversed flow was seen considerably further upstream on the shark skin surface, although the height of the lowest-value contour line (5%) was approximately the same on both surfaces. The highest-value contour line seen at this angle of attack on either surface was 15%, beginning at $x/c=0.938$ for the shark skin and $x/c=0.987$ for the painted surface. When the angle of attack was raised to 12 degrees, the percentage of time that the reversed flow reached the threshold value near the trailing edge increased significantly. Contour lines of 50% were seen over both surfaces. The region of 10% free stream reversed flow extended into the Location 4 measurement window for the shark skin surface, with the first contour line seen at $x/c=0.801$. The 5% line was measured at $x/c=0.869$ on the painted surface. The height of the 5% line at the trailing edge was similar in both cases at this angle of attack.

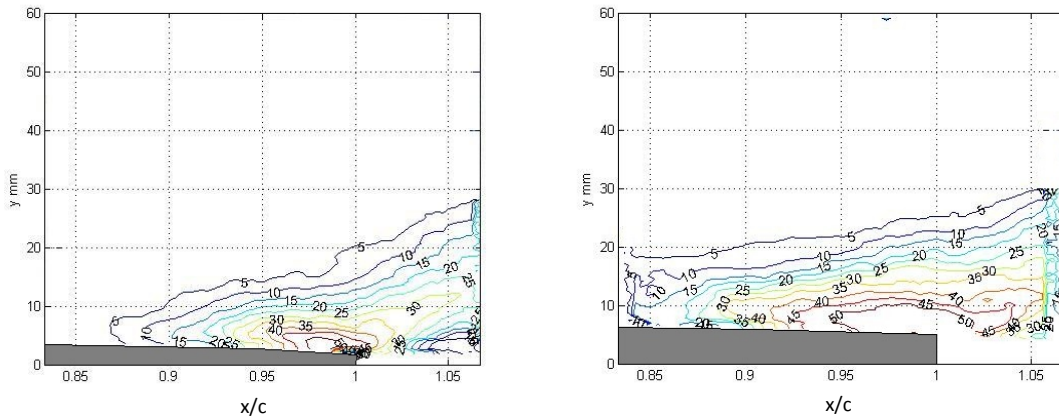


Figure 4.6 10% free stream backflow coefficient contours, $Re=100,000$, $\alpha=12^\circ$, Location 5.
Painted surface (left) vs. shark skin (right).

The results at $\alpha=16^\circ$ showed the same reversal in the trend developed at the lower angles as shown by the backflow coefficient results discussed previously. While the total chordwise length of the 10% free stream backflow region was similar for both surfaces, large regions of significantly higher-value contour lines were observed in the flow above the painted surface. In two separate regions close to the surface, one each in Locations 4 and 5, the backflow was measured to reach a magnitude of at least 10% of the free stream velocity over half of the time. On the shark skin surface, the highest-value contour lines observed were 30%, and these only occurred in two very small regions. Over much of the shark skin at Locations 4 and 5, the highest contour values measured were 20%. In addition, over the entire region of reversed flow, the average height of the area in which 10% free stream backflow was seen was much lower for the shark skin surface than for the painted surface. These results seem to show that, at a post-stall angle of attack, the reversed flow in general achieves high magnitudes close to the surface a considerably smaller percentage of the time with the shark skin applied to the hydrofoil. The contour plots displaying these results for $\alpha=16^\circ$ are shown below in Figure 4.7.

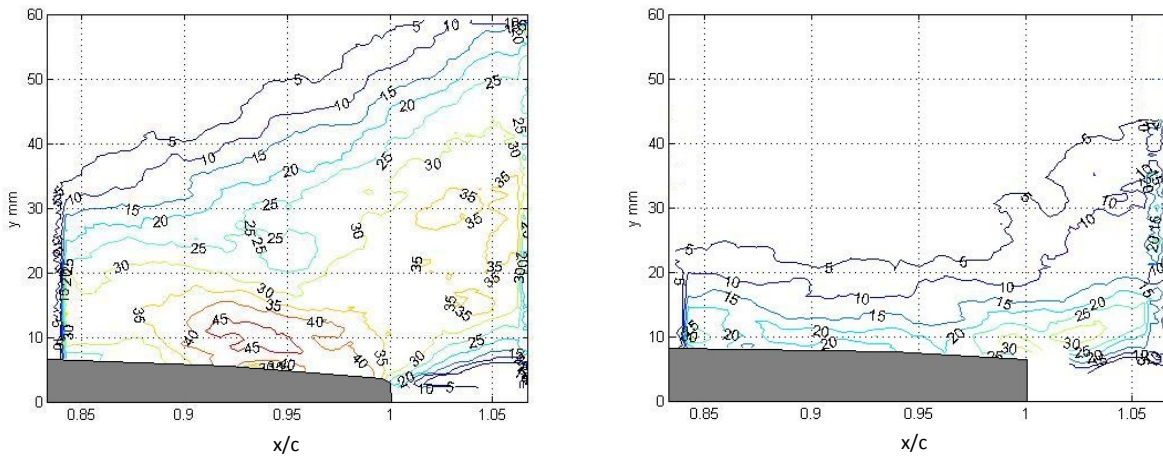


Figure 4.7 10% free stream backflow coefficient contours, $Re=100,000$, $\alpha=16^\circ$, Location 4.
Painted surface (left) vs. shark skin (right).

4.4 AVERAGE AND PEAK BACKFLOW MAGNITUDE

Contours of the average magnitude of the reversed flow were created in all experimental cases where backflow was observed. For each case, the backflow magnitude was averaged over the total number of instantaneous velocity vectors showing reversed flow at each separate vector location within the processing grid. Because of this, the number of vectors averaged at each point was not necessarily the same, and was in most cases much greater in areas within the separated region close to the surface than in those on the fringes of the region of backflow. The peak backflow magnitude was also calculated for each vector location within the flow field for the same cases.

For the cases run at $Re=100,000$, similar values of average backflow magnitude were measured at $\alpha=8^\circ$ and $\alpha=10^\circ$ for both configurations within the region of at least 10% backflow established by the backflow coefficient graphs. In this region, the highest average backflow magnitudes observed were approximately 2.0 cm/s for the painted surface and 3.0 cm/s in small areas over the shark skin surface. Much higher values (up to 8.0 cm/s) of average backflow magnitude were measured above the established region of backflow. However, backflow at these heights above the surface occurred less than 10% of the time, so any high-speed reversed flow was likely due to fast-moving, larger-scale vortices taking place in the outer flow region. At $\alpha=12^\circ$, higher values of average backflow magnitude were seen in the region near the trailing edge. For the painted surface, a maximum average magnitude of 4.0 cm/s was measured starting at $x/c=0.925$, while a region of backflow magnitude in the range of 5.0 cm/s was observed to begin at approximately $x/c=0.895$, with smaller patches of reversed flow of this magnitude occurring separately at other points within the separated region. As was the case with the lower angles of attack, much higher average magnitudes are seen outside of this region, however flow

reversal is occurring at these locations a very small percentage of the time. The comparison of the average backflow magnitude for the two surfaces at $\alpha=12^\circ$ is displayed below in Figure 4.8.

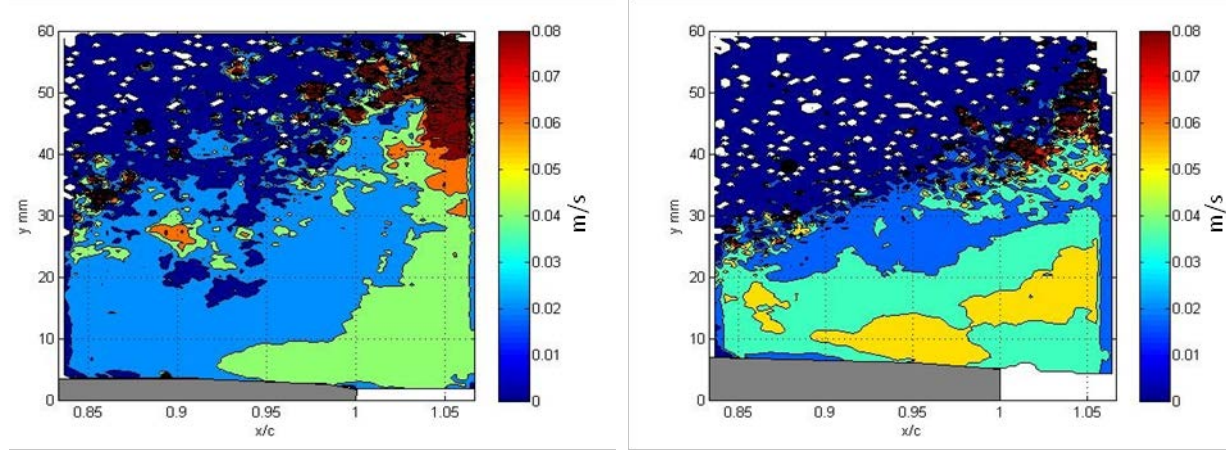


Figure 4.8 Average backflow magnitude contour, $Re=100,000$, $\alpha=12^\circ$, Location 5. Painted surface (left) vs. shark skin (right).

For the same Reynolds number, the average backflow magnitude was seen increase dramatically over the painted surface at $\alpha=16^\circ$ compared to the first three angles of attack. Large areas of backflow with magnitudes of 6-7 cm/s filled a significant portion of the separated region downstream of $x/c=0.75$, and magnitudes of 4.0 cm/s were seen up to the very front of the backflow region at $x/c=0.6$. These high values were seen very close to the surface spanning from $x/c=0.8$ to the trailing edge. In the case of the shark skin surface, no such high magnitudes were observed in the backflow region. Small patches of backflow with an average magnitude in the range of 4.0 cm/s, but the backflow over most of the surface from $x/c=0.73$ to the trailing edge averaged a magnitude of approximately 3.0 cm/s. These results seem to agree well with the graphs of 10% free stream backflow. The difference between the two surfaces can be seen in the contour plots in Figure 4.9.

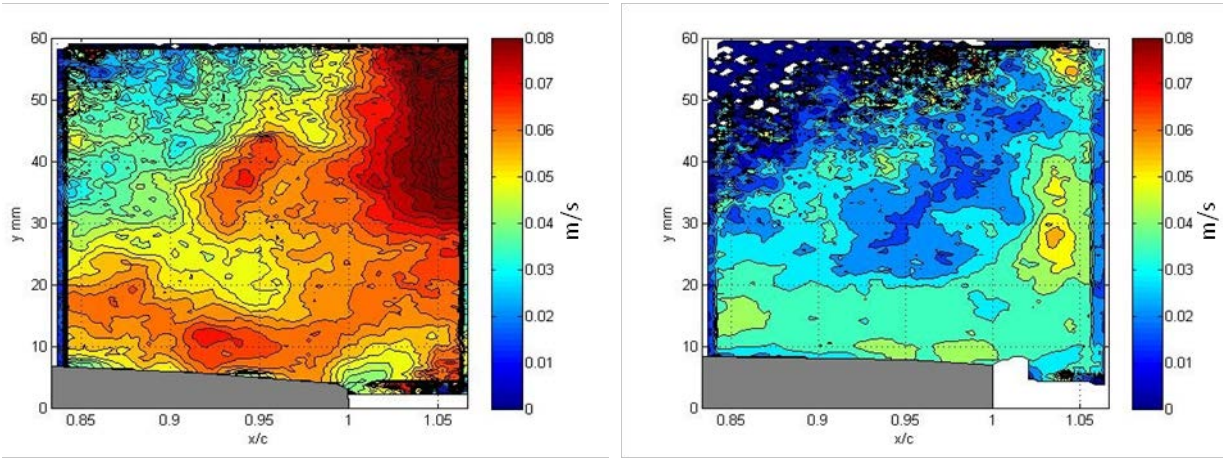


Figure 4.9 Average backflow magnitude contour, $Re=100,000$, $\alpha=16^\circ$, Location 5. Painted surface (left) vs. shark skin (right).

There was considerably less difference between the peak backflow magnitude plots of the different cases. The peak magnitude varied widely within the separated region at all angles of attack, with small patches of very high magnitude backflow (greater than 60 cm/s, on the same order as the upper edge positive u velocity) occurring randomly in all cases. Since these bursts of very high-speed reversed flow could occur at any point within the 12-second measurement time, they are likely the result of large-scale vortices moving through the backflow region. However, the sizes of these patches of high-magnitude backflow were observed to be significantly smaller on average for the shark skin than for the painted surface at $\alpha=16^\circ$. Sample plots of the peak backflow magnitude are shown in Figure 4.10.

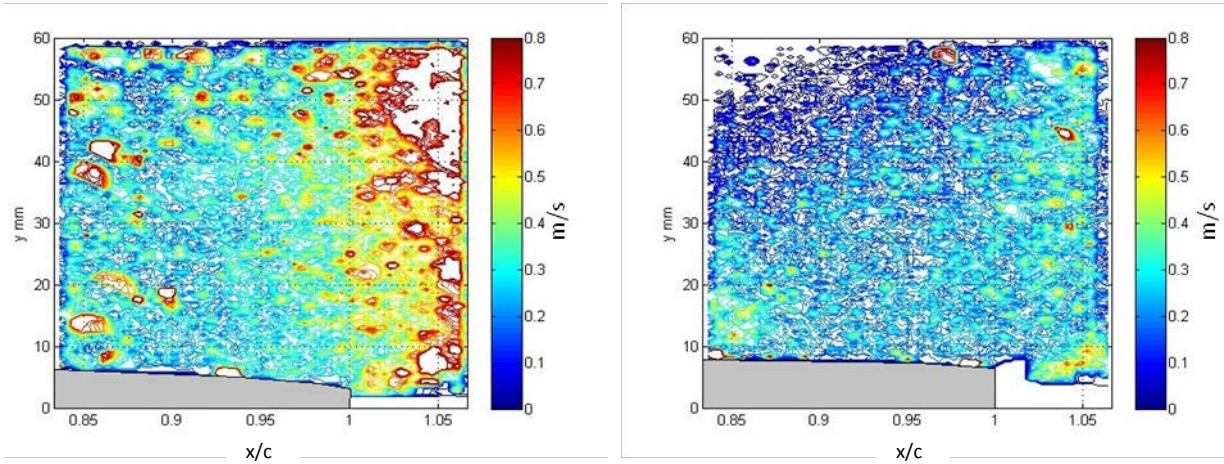


Figure 4.10 Peak backflow magnitude contour, $Re=100,000$, $\alpha=16^\circ$, Location 4. Painted surface (left) vs. shark skin (right).

4.5 INSTANTANEOUS VELOCITY VS. TIME

The instantaneous values of streamwise velocity at individual points approximately 5 mm above the surface were plotted versus time for two locations each at $\alpha=12^\circ$ and $\alpha=16^\circ$ for the $Re=100,000$ cases on both surface configurations. At $\alpha=12^\circ$, a point at $x/c=0.85$ from Location 4 and a point at $x/c=0.95$ from Location 5 were investigated. At $\alpha=16^\circ$, points at $x/c=0.75$ and $x/c=0.95$ were used, also located 5 mm from the hydrofoil surface. These instantaneous velocity values were measured at each time step over the total 12 seconds of run time for each case, for a total of 4800 data points each.

The time history plots for $\alpha=12^\circ$ at the 85% chord location show local peaks of velocity typically reaching values of 15-20 cm/s. However, only one large event of flow reversal is seen for the painted surface, whereas at least four such events are seen in the case of the shark skin. These periods of reversed flow peak at approximately -7 to -9 cm/s for most events. At the 95% chord location (Figure 4.11), the local backflow peaks increased to values of -10 to -12 cm/s, while the average positive-direction peaks was reduced to a range of 10-15 cm/s. One notable difference at this location was that, even though the total time of reversed flow was greater for

the shark skin surface, the frequency of flow direction change appeared much lower. The backflow primarily occurred in several large events spanning approximately 1.5 seconds each, as opposed to the painted surface where the direction of the flow changed many times in rapid succession.

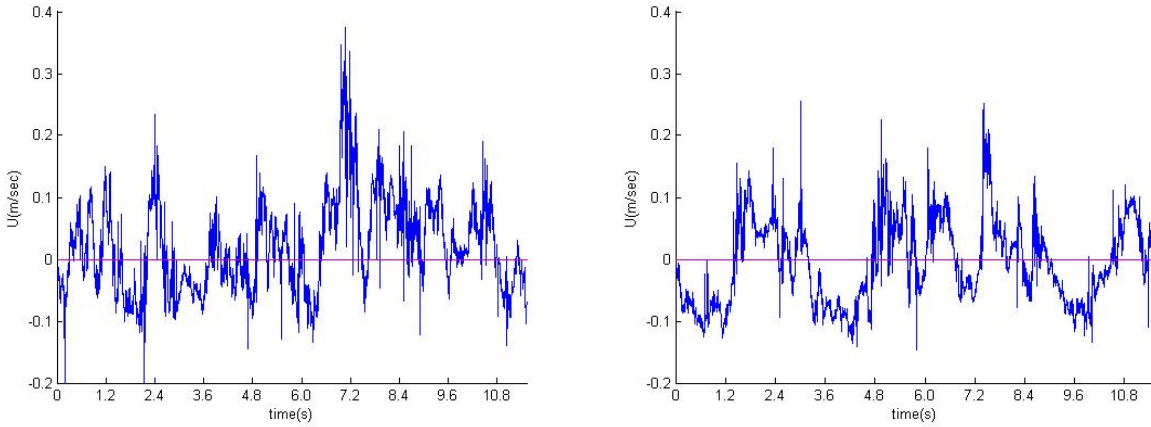


Figure 4.11 Instantaneous velocity history, $Re=100,000$, $\alpha=12^\circ$, 95% chord. Painted surface (left) vs. shark skin (right).

This phenomenon of lower fluctuation frequency was also observed at the 75% chord location for the $\alpha=16^\circ$ case. The velocity time history for the painted surface fluctuated rapidly with reversed flow peaks in the range of -15 cm/s. The reversed flow over the shark skin surface was measured to mostly peak below -10 cm/s, and most of the backflow occurred in discrete events with a duration on the order of 0.5 seconds. At 95% chord, the flow at the point selected on the painted surface was seen to spend the majority of the time reversed, with some backflow events lasting for 2 seconds or longer. For the shark skin surface, the periods of backflow were much shorter in duration with lower peaks, resulting in a significantly smaller total time of reversal. These results support the hypothesis that once localized backflow of sufficient momentum is initiated, the scales in the affected area are bristled due to the reverse shear and

obstruct the reversed flow from reaching a higher magnitude and pushing further upstream. The time history plots for $\alpha=16^\circ$ at $x/c=0.95$ are compared in Figure 4.12.

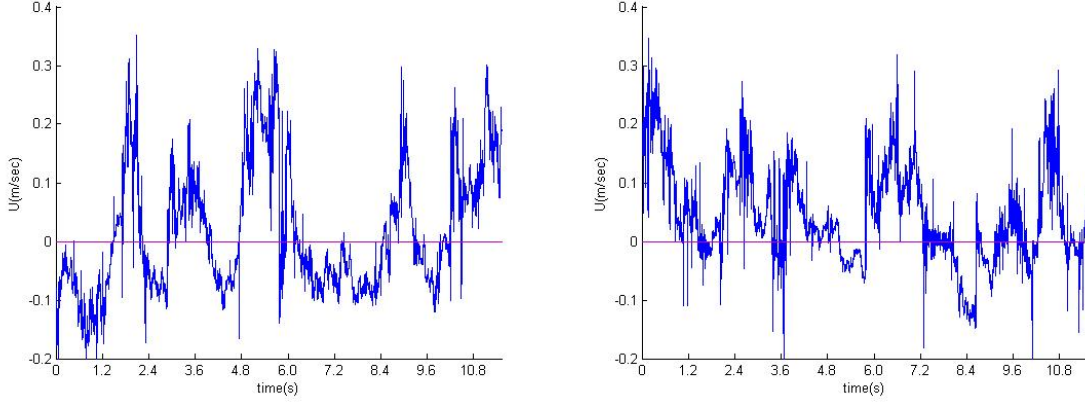


Figure 4.12 Instantaneous velocity history, $Re=100,000$, $\alpha=16^\circ$, 95% chord. Painted surface (left) vs. shark skin (right).

4.6 RESULTS FOR MEASUREMENT PLANES AT 75% DEPTH

Data was obtained at $\alpha=10^\circ$ and $\alpha=12^\circ$ in a measurement plane near the trailing edge at 75% depth to observe the changes from the mid-depth measurement plane due to three-dimensionality in the flow. Backflow coefficient plots showed that, in all cases run at this depth, the size of the backflow region was smaller than what was seen at the mid-span plane. At $Re=100,000$ and $\alpha=10^\circ$, the region of reversed flow was measured to be slightly shorter on the shark skin surface, with the point of ITD occurring at $x/c=0.95$ compared to $x/c=0.9$ for the painted surface. 50% backflow was not measured on either surface under these conditions. The height of the 10% backflow contour line at the trailing edge was approximately 8 mm for both surfaces, very close to the values seen at the primary mid-depth measurement plane for this angle of attack. These backflow coefficient contours can be seen in Figure 4.13. The plots of the u -

velocity field were also very similar to those generated at the trailing edge location at mid-depth, and no significant differences were observed between the two surfaces in these graphs. Contours of average backflow magnitude showed similar values within the backflow regions of both surfaces, although higher average magnitude values were seen in the outer flow region of the shark skin surface.

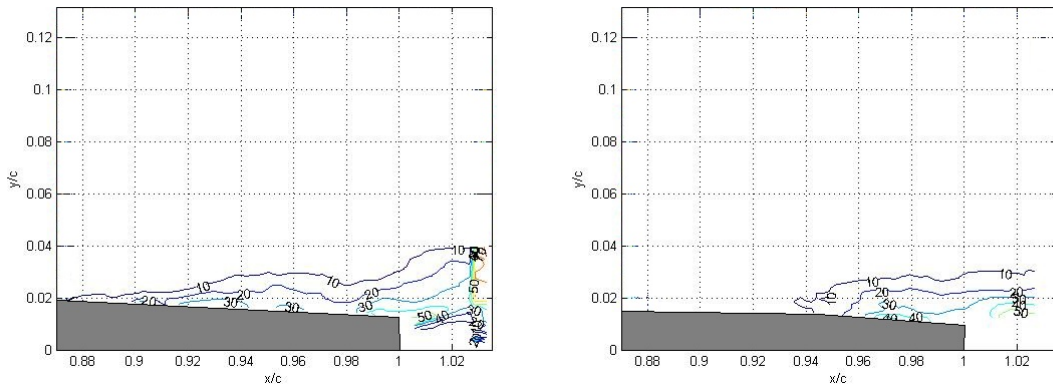


Figure 4.13 Backflow coefficient contours, $Re=100,000$, $\alpha=10^\circ$, trailing edge, 75% depth.
Painted surface (left) vs. shark skin (right).

For the $\alpha=12^\circ$ cases, the shark skin surface was again observed to generate a shorter region of low-percentage backflow, with the point of ITD being measured at $x/c = 0.945$ compared to $x/c=0.875$ on the painted surface, as shown in Figure 4.14. However, the point of detachment was determined to be approximately $x/c=0.97$ on both surfaces, and similar thicknesses were seen for the backflow region of each. The average backflow magnitude was considerably higher near the trailing edge of the shark skin surface, with values in the range of 3.5 cm/s compared to approximately 1.0 cm/s for the painted surface. The time-averaged velocity fields of the two surfaces at this angle of attack were nearly identical. The results of the measurement plane at this greater depth show the effect of the three-dimensionality present in the flow, and the reduced size of the backflow region could be contributed to a less-adverse pressure

gradient, as this location is farther from the influence of the water-air surface interaction at the top of the test section.

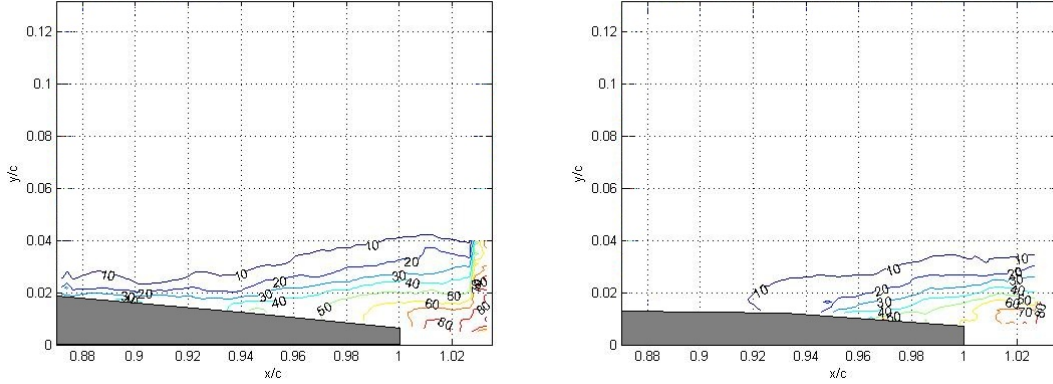


Figure 4.14 Backflow coefficient contours, $Re=100,000$, $\alpha=12^\circ$, trailing edge, 75% depth.
Painted surface (left) vs. shark skin (right).

4.7 RESULTS FOR 50 CM/S FREE STREAM VELOCITY

All experiments carried out with the free stream speed of 32 cm/s and $Re=100,000$ were also conducted with $U = 50\text{cm/s}$ and a Reynolds number of 152,000 for the same cases. However, examination of instantaneous velocity fields from the runs taken at this free stream speed showed multiple, large regions of invalid vectors (and resulting zero-value placeholders) being generated in a majority of the images. A sample image of these invalid regions is shown in Figure 4.15. While regions of invalid velocity values were also observed to occur occasionally in the cases run at $U = 32\text{ cm/s}$, the number of valid data points for each 4800-image case remained above 4500 for most vector points within the backflow region at all angles of attack. The data obtained in Locations 1 and 2 at $Re=152,000$ was not subject to this same degree of error, however little information about the behavior of the separated flow could be gathered from these measurement locations. In the cases run at $U = 50\text{ cm/s}$ the number of valid data point at the individual grid locations in the backflow region was seen to decrease sharply, from

approximately 4400 very close to the surface to less than 2500 halfway up the height of the measurement window. With up to 50% of the collected data producing invalid data points, the results from these experiments could not be discussed with any degree of certainty. Although less than 10% of the data points within the first 5-8 mm above the surface were determined to be invalid, the thickness of the backflow region was observed to be much larger than this, and to attempt to compare only partially valid results against the results of the $Re=100,000$ cases would be erroneous. Nevertheless, the backflow coefficient contours for both surfaces at $\alpha=16^\circ$, Location 5 are shown in Figure 4.16.

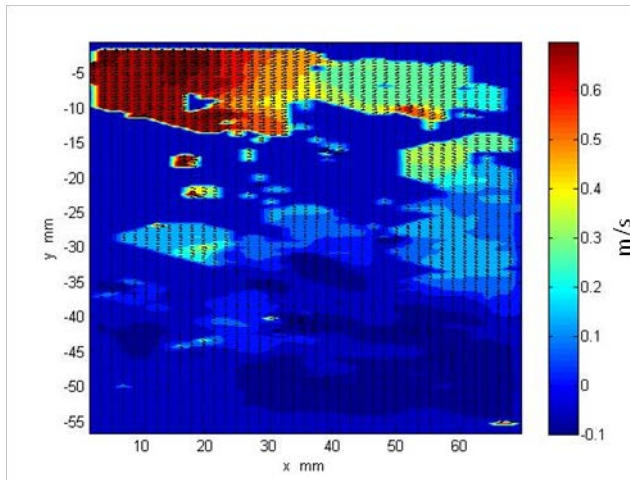


Figure 4.15 Instantaneous u field, $Re=152,000$, $\alpha=16^\circ$, Location 5 showing incomplete vector grid (zero velocity regions denote invalid vectors).

This phenomenon was very likely due to the existence of strong spanwise fluid motion which was much less prominent at the lower free stream speed. Inspection of the raw PIV images showed that at many times large groups of particles would enter or exit the measurement plane over the span of two or three consecutive images, making it extremely difficult for the processing software to track their movement accurately. In these instances, the software would replace the bad data with filler value, which would be averaged into the mean velocity field as a point of zero velocity. These points were simply thrown out by the backflow programs and not counted as

a part of the total average. For these reasons, although all preliminary PIV data was obtained for the 50 cm/s runs, further analysis of the backflow at this speed was stopped when it became clear that the results could not be accurately compared to those found at $U = 32$ cm/s.

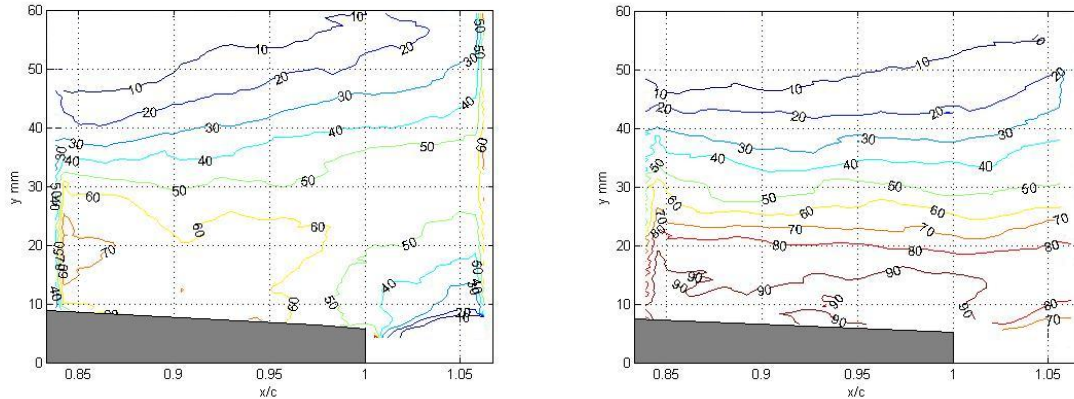


Figure 4.16 Backflow coefficient, $Re=152,000$, $\alpha=16^\circ$, Location 5. Painted surface (left) vs. shark skin (right).

4.8 DETERMINATION OF TURBULENCE

As described before, the flow over the hydrofoil model was tripped in all experiments by a 2mm diameter copper tube placed across the span of the model at an x-location of 5% chord. The location and size of the boundary layer trip was chosen as a result of preliminary calculations and several previous experiments, which used smaller-diameter copper tubes that failed to maintain a fully turbulent boundary layer. The presence of a turbulent boundary layer over the upper surface of the hydrofoil model was analyzed by calculating the x-direction

turbulence intensity percentage (defined as —————) for the processed vector fields in each case as well as determining the degree of fluctuation of streamwise velocity with time over the course of each run.

In all experimental cases, the turbulence intensity percentage was found to reach a maximum just after the trip and decrease rapidly to an approximately constant value throughout the boundary layer over the rest of the surface. Turbulence intensity calculations for the boundary layer in the measurement windows upstream of the onset of separation were observed to hold a relatively steady value of approximately 2-3 times the turbulence intensity observed in the free stream flow above the hydrofoil model surface.

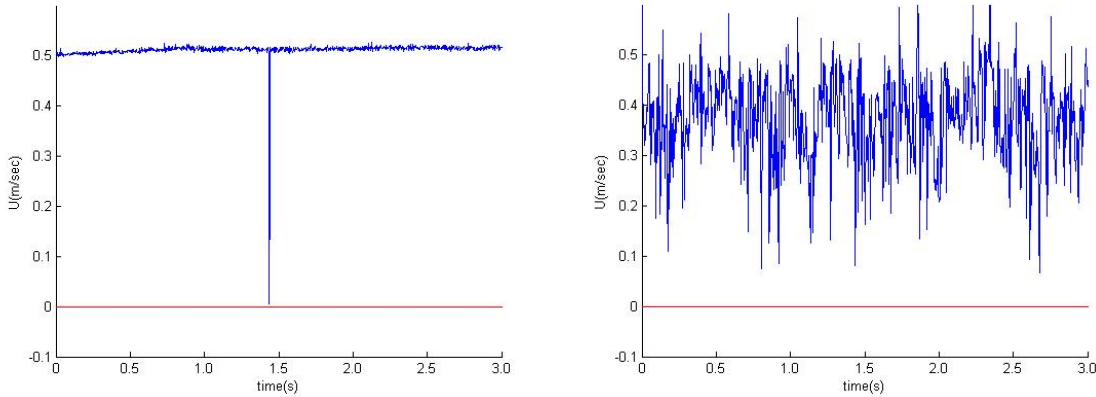


Figure 4.17 Instantaneous velocity history, $Re=100,000$, $\alpha=10^\circ$, 30% chord. Outer flow region (left) vs. 5 mm above hydrofoil surface (right).

Instantaneous velocity histories were plotted at individual points in the boundary layer at locations of $x/c=0.30$, $x/c=0.60$, and $x/c=0.75$, for the two lower angles of attack (8 and 10 degrees), approximately 5 mm above the surface. Velocity histories were also generated for the same streamwise locations at a height far outside of the boundary layer as a point of reference. Instantaneous fluctuations of at least 20% of the average streamwise velocity were seen at the points inside the boundary layer, while fluctuations of approximately 1-2% of the average velocity were seen at the points in the outer flow above the hydrofoil. Based on these measurements, we believe we can confidently say that the trip used in these experiments results in a fully turbulent boundary layer over the upper surface of the hydrofoil.

4.9 COMPARISON OF AVERAGES

Two additional 1200-image runs were taken for all angles of attack on the shark skin surface at Location 5. This was due to preliminary results from a separate experiment which showed that 4800 images, or 12 seconds of flow data, may not be enough to reach a time-averaged flow field. For this reason, average values of the u-velocity field, backflow coefficient, and average backflow magnitude were plotted for both 5 runs (6000 images) and 6 runs (7200 images) for Location 5 at 8 and 16 degrees. The results were compared to the standard 4800-image averages taken for the same cases. The comparison of the backflow coefficient contours at $\alpha=16^\circ$, Location 5 on the shark skin surface for 4800 images and 7200 images (Figure 4.18) show few differences between the overall size and profile of the backflow region with the increased duration of the run. With the increase in the number of images, the point of detachment on the surface was measured to move less than 1 mm, and the thickness of the backflow region at the trailing edge differed by less than 2 mm between the two averages. The results at $\alpha=8^\circ$ show a variation in the location of ITD by approximately 1 mm and a change in h_{sr} of less than 1 mm at the trailing edge. Similarly matching results were seen for the plots of average velocity and backflow magnitude. Thus it can be reasonably concluded that 4800 images results in a sufficient average for the flow conditions present in these experiments.

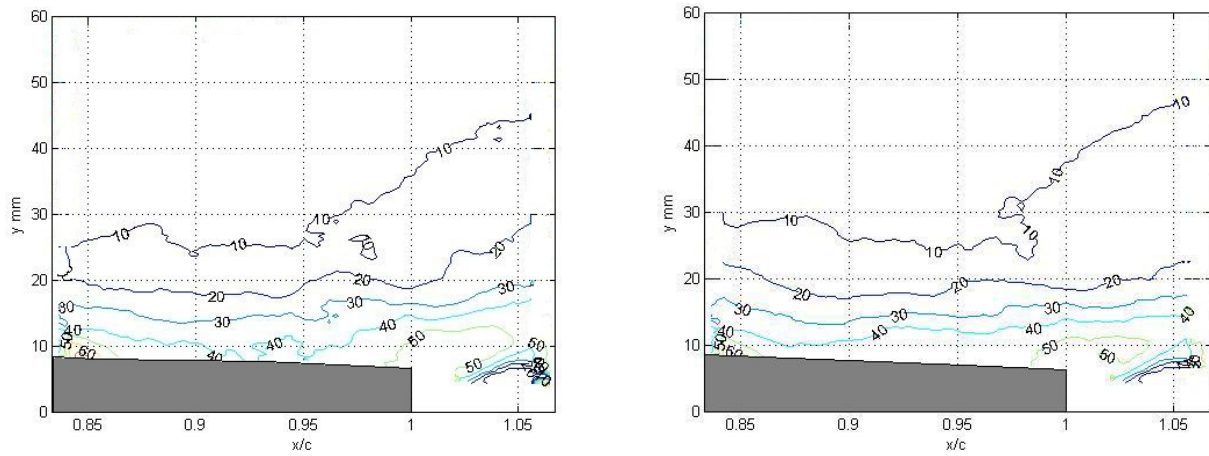


Figure 4.18 Comparison of backflow coefficient, $Re=100,000$, $\alpha=16^\circ$, Location 5, 4800-image average (left) vs. 7200-image average (right).

5. CONCLUSIONS

5.1 SEPARATION CONTROL EFFECTS OF SHARK SKIN

The results of this study showed a distinct difference between the characteristics of the separated flow over the hydrofoil model with a painted, sanded surface and the same model with the mako skin samples attached, in the cases where the Reynolds number was held at 100,000. At the three lower angles of attack studied in these experiments, analysis of the backflow region showed that the differences between its size, average magnitude, and the amount of time it produced high-velocity reversed flow for the two surface configurations was relatively small. However, the shark skin surface did produce measurably more adverse results, most notably in the form of more upstream locations of the points of ITD and detachment. These differences in backflow were observed to occur with very little change to the time-averaged velocity field over the surface.

The tests run at the highest angle of attack showed very different results. A significant reduction was observed in both the average thickness and magnitude of the separated region when the mako skin was applied to the surface. Although the total length of the backflow region based on the 10% backflow contour line was nearly the same for both surface at this angle of attack, the distance from the point of detachment to the trailing edge was reduced by 27% through employment of the shark skin. In addition, the amount of time that the reversed flow was higher than 10% of the free stream velocity was 40% less for the shark skin than for the painted surface. Also, the instantaneous velocity history plots showed that on average, each flow reversal

event had a considerably shorter duration in the case of the shark skin surface. These results showed strong evidence that, at $Re=100,000$ and $\alpha=16^\circ$, the scales located within the backflow region have indeed bristled and created a partial-slip condition due to the cavities formed between the scales. This was supported by the measurement of significantly higher average backflow magnitudes over the painted surface compared to what was observed at the lower angles of attack, which seemed to show that between $\alpha=12^\circ$ and $\alpha=16^\circ$, the backflow produces a threshold reverse-direction shearing stress below which the scales do not generate cavity vortices. This idea of a threshold shear would also explain the negative effects of the shark skin at the lower angles of attack; as the scales would not bristle fully, and merely disrupt the flow and increase the drag over the surface, supporting the measurements of higher drag over slightly-bristled shark scales by Bechert (2000). However, since the initial aim of this study was to focus primarily on moderate, pre-stall angles of attack, no tests of angles between 12 and 16 degrees were run; 16 degrees was viewed as an "extreme" case. Therefore, additional experiments would be necessary to determine the exact angle at which the scales become beneficial in terms of separation reduction at this Reynolds number.

It is important to note that, due to the ridge in the center shark skin sample, the results for the two surface configurations were not obtained at the exact same plane of depth and are therefore subject to the effects of three-dimensional flow. Approximately 1 inch (2.54 cm) separated the two measurement planes. However, since a negative effect was observed for the shark skin at the lower angles of attack and a positive effect was seen at the highest, it could be reasonably concluded that the difference in depth of the two planes did not introduce a bias into the results, even if the exact values of the backflow variables was altered by this discrepancy. In addition, irregularities in the trailing edge of the skin sample could be responsible for some of

the differences in the backflow over the two models. A fresh model, with more uniform skin samples cut with more precise equipment, would be necessary to eliminate these sources of uncertainty.

5.2 REYNOLDS NUMBER DEPENDENCY

Due to the poor PIV results for the tests run at $Re=152,000$ discussed earlier, the changes in the backflow with increased free stream velocity were not able to be fully analyzed. These results show that the current configuration of the water tunnel is insufficient for conducting tests at maximum velocity without severe three-dimensional effects. To reduce the three-dimensionality of the flow, the surface interaction between the water and air at the top of the water tunnel would have to be negated by mounting a solid surface along the top of the test section so that the flow would be totally enclosed.

Since the mako shark typically swims at a much higher speed than was possible in these tests, the scales on the shark's flank would operate in a flow with a Reynolds number at least an order of magnitude higher than that which was achieved in this study. As a result, experiments including a larger variation of Reynolds than could be produced in this water tunnel should be conducted to accurately document the Reynolds number dependency of the scales' flow control mechanisms. As the necessary facilities become available, tests at much higher Reynolds numbers (10^6 or higher) would be very beneficial in determining the effects of the shark skin in flow with a significantly smaller viscous length scale, as would be seen under normal swimming conditions.

5.3 FUTURE WORK

As discussed previously, tests run at $Re=100,000$ at additional angles attack, both in the 13-15 degree range and greater than 16 degrees, would provide additional insight into the effectiveness of the shark skin's flow control mechanisms with varying pressure gradients. To investigate the Reynolds number dependency, an intermediate free stream speed in the range of 40 cm/s could potentially yield useful data without inducing the large amount of three-dimensional flow seen at 50 cm/s. An increase in the resolution of the PIV vector grid would be valuable at key locations such as the points of detachment; this could be achieved by increasing the zoom of the camera so that the measurement window covers a smaller region. A significantly more zoomed-in view would be necessary to observe the actual motion of the scales in the flow. Future experiments are planned which will use a localized jet to determine the reversed flow velocity, and ultimately the shear, necessary to bristle the scales.

Continuing experiments with volumetric 3D velocimetry are being conducted to analyze the boundary layer separation in a three-dimensional region over the NACA 4412 hydrofoil, both with initially laminar and fully turbulent boundary layers. The low processing resolution of this system close to the surface is currently prohibitive to the complete analysis of the 3D separated region, however new camera lenses allowing for a greater resolution are being developed and will be implemented soon. Ultimately, the V3V system may allow for the flow field analysis of shark skin on an airfoil in a wind tunnel, which could produce Reynolds numbers in the range of those experienced by a swimming shark, and therefore more closely replicate the flow conditions under which the scales operate in nature.

REFERENCES

- Badran, O.O. & Bruun, H.H. 2003. Turbulent flow over a NACA 4412 airfoil at angle of attack 15 degree. *4th Joint Fluids Eng. Conf. Honolulu, Hawaii.*
- Bechert, D. W., Bruse, M., Hage, W. & Meyer, R. 2000. Fluid mechanics of biological surfaces and their technological application. *Naturwissenschaften* 80:157-171
- Bourgoyné, D.A., Ceccio, S.L., Dowling, D.R., Jessup, S., Park, J., Brewer, W. & Pankajakshan, R. 2001. Hydrofoil turbulent boundary layer separation at high Reynolds numbers. *Proc. 23rd Symp. on Naval Hydrodyn. Val de Reuil, France.*
- Bushnell, D. 1983. Turbulent drag reduction for external flows, *AIAA Paper 83-0227*
- Djenidi, L., Anselmet, F. & Antonia, R. 1999. The turbulent boundary layer over transverse square cavities. *J. Fluid Mech.* 395:271-294
- Gad-el-Hak, M. 2000. Flow Control: Passive, Active and Reactive Flow Management. Cambridge University Press, Cambridge, UK.
- Howard, F. & Goodman, W. 1985. Axisymmetric bluff-body drag reduction through geometrical modification. *J. Aircraft* 22:516-522.
- Lang, A. & Hidalgo, P. 2009. Cavity Flow Characterization of the Bristled Shark Skin Microgeometry. *AIAA-2009-1107*
- Lang, A., Motta, P., Hueter, R. Habegger, M.L. & Afroz, F. 2011. Shark skin separation control mechanisms. *Marine Tech. Soc. J.* 45(4):208-215
- Lin, J. 2002. Review of research on low-profile vortex generators to control boundary-layer separation. *Prog. in Aero. Sci.* 38:389-420
- Manhart, M. & Friedrich, R. 2002. DNS of a turbulent boundary layer with separation. *Int. J. Heat and Fluid Flow.* 23:572-581
- Meyer, R., Hage, W., Bechert, D., Schatz, M., Knack, T. & Thiele, F. 2007. Separation control by self-activated movable flaps. *AIAA Journal*, 45(1):191-199
- Na, Y. & Moin, P. 1998. Direct numerical simulation of a separated turbulent boundary layer. *J. Fluid Mech.* 374:379-405

- Savill, A. 1988. A flow visualization investigation of turbulent boundary layer structure over micro air bearing surfaces including effect of outer layer manipulation. *2nd Int. Symp. on Fluid Control, Measurement Mech. and Flow Vis.* p.430-436
- Schlichting, H. 1979. Boundary-Layer Theory, 7th ed. McGraw-Hill, New York, NY. pp. 555-595
- Simpson, R.L. 1989. Turbulent Boundary Layer Separation. *Ann. Rev. Fluid Mech.* 21:205-234
- Simpson, R.L. 1997. Aspects of Turbulent Boundary-Layer Separation. *Prog Aerospace Sci.* 32:457-521
- Videler,J. 1995. Body surface adaptions to boundary-layer dynamics. *Symp. of the Soc. for Exp. Bio.* 49:1-20
- Willert, C.E. & Gharib, 1991. M. Digital image particle velocimetry. *Experiments in Fluids* 10, 181-193.

APPENDIX - UNCERTAINTY ANALYSIS

The time-resolved particle image velocimetry experimental technique produces several sources of uncertainty in the calculation of the flow velocity, which should be noted. First, a degree of error is introduced if the seeding particles are not perfectly neutrally buoyant and therefore do not follow the path of the flow exactly. For the actual PIV processing itself, Willert and Gharib (1991) noted an approximately 1% uncertainty in the calculation of particle displacement and the resulting velocity. An additional source of uncertainty in the determination of correct displacement is the manual length scale calibration. In this calibration, the total number of pixels was measured between marks 2 cm apart on a ruler placed in the measurement plane. Estimating a variation of 5 pixels for the correct location of each end mark results in an error of approximately 1.4% in the calculated particle displacement, based on the total calibration length measured. Due to the height over which a single vector is calculated (16 pixels), measurements at the defined surface of the hydrofoil in the PIV processing software produce an uncertainty of 3.0% (\pm one vector grid height with respect to the total image height). The maximum uncertainty in the measurement positions due to the changes in angle of attack is approximately 2.9%. The combination of these sources of error results in an estimated 5% uncertainty in the values of the velocity vectors calculated by the PIV software.

In addition to the uncertainty in the actual calculation of the particle displacement and velocity, the error resulting from the averaging scheme used to determine the various backflow contours should also be discussed. Due to the occasional production of localized, invalid vectors

by the PIV software (as a result of insufficient instantaneous seeding or excessive three-dimensional flow), the averages of backflow coefficient and average backflow magnitude are only calculated out of the total number of valid vectors for each grid location in each case. Therefore, the total number of values over which these parameters were averaged was less than 4800, and the number by which the total was reduced varied with each processing grid location. In a sampling of the total number of valid data points at each grid location in the Location 5 measurement window at $\alpha=16^\circ$, it was found that the number of valid velocity values ranged from 4500 to 4700 at grid points within the backflow region. This is a maximum difference of 6.25% from a true average of 4800 images, so the value obtained through this averaging could vary by as much. To reduce the effects of this source of error, additional steps would need to be taken in the experimental setup to minimize three-dimensional flow over the model.